1 **Pattern formation and bistability in a synthetic intercellular genetic toggle**

2

3 Bárbara de Freitas Magalhães[1,5], Gaoyang Fan[2,5], Eduardo Sontag[3], Krešimir Josić[2,*], Matthew

4 R. Bennett[1,4,*]

5 1. Department of Biosciences, Rice University, Houston, TX, USA

6 2. Department of Mathematics, University of Houston, Houston, TX, USA

7 3. Department of Bioengineering, Department of Electrical and Computer Engineering,

8 Northeastern University, Boston, MA, USA

9 4. Department of Bioengineering, Rice University, Houston, TX, USA

10 5. These authors contributed equally

11 *Correspondence: josic@math.uh.edu; matthew.bennett@rice.edu

12

13 <u>**Summary**</u>

14

15 Differentiation within multicellular organisms is a complex process that helps to establish spatial

16 patterning and tissue formation within the body. Often, the differentiation of cells is governed by

17 morphogens and intercellular signaling molecules that guide the fate of each cell, frequently

18 using toggle-like regulatory components. Synthetic biologists have long sought to recapitulate

19 patterned differentiation with engineered cellular communities and various methods for

20 differentiating bacteria have been invented. Here, we couple a synthetic co-repressive toggle

21 switch with intercellular signaling pathways to create a "quorum-sensing toggle." We show that

22 this circuit not only exhibits population-wide bistability in a well-mixed liquid environment, but

23 also generates patterns of differentiation in colonies grown on agar containing an externally

24 supplied morphogen. If coupled to other metabolic processes, circuits such as the one

25 described here would allow for the engineering of spatially patterned, differentiated bacteria for

26 use in biomaterials and bioelectronics.

27

28 <u>**Keywords**</u>

29 Genetic toggle switch, quorum sensing, pattern formation, self-organization, synthetic biology.

30

31 <u>**Introduction**</u>

32 One goal of synthetic biology is the creation of engineered biological systems that can perform a

33 wide variety of functions (Benner & Sismour, 2005; Cameron et al., 2014; Cheng & Lu, 2012;

34 Church et al., 2014). Such systems could be used for various environmental, industrial, and

35   medical applications (Callura et al., 2012; Khalil & Collins, 2010; McCarty & Ledesma-Amaro,

36   2019; Xia et al., 2019). However, synthetic biology is also advancing basic research by

37   providing a bottom-up approach to understanding phenomena governed by nontrivial genetic

38   regulatory mechanisms. This is done by creating and perturbing "synthetic gene circuits" in

39   living systems that behave similarly to their natural counterparts and can thus serve as a model

40   systems (Davies & Glykofrydis, 2020; Weisenberger & Deans, 2018).

41   As part of the ground up approach to basic research, synthetic biologists have long

42   sought to use engineered cells to recapitulate spatial patterns seen in multicellular systems

43   (Cachat et al., 2017; Davies & Glykofrydis, 2020; Grant et al., 2020; Kim et al., 2020; Santos-

44   Moreno & Schaerli, 2018; Sekine et al., 2018). Many mechanisms have been proposed to

45   explain the appearance of natural patterning, such as the reaction-diffusion model (Turing,

46   1952) and the positional information model (or French flag model) (Wolpert, 1969). These

47   mechanisms have been used as blueprints for synthetic analogs of biological patterns (Diambra

48   et al., 2015; Karig et al., 2018a; Sekine et al., 2018). Scientists are also working towards self-

49   organizing patterns (Cachat et al., 2017; Cao et al., 2016; Curatolo et al., 2020; Liu et al., 2011;

50   Payne et al., 2013; Potvin-Trottier et al., 2016; Santos-Moreno & Schaerli, 2018) that use

51   intercellular signals to regulate transcriptional activity (Cao et al., 2016; Curatolo et al., 2020; Liu

52   et al., 2011; Payne et al., 2013).

53   Indeed, the circuit topology of the first synthetic gene circuit to be described, the "genetic

54   toggle switch" (Gardner et al., 2000a), has also been implicated in spatial patterning. The toggle

55   switch is comprised of just two repressors that regulate each other's promoters – and it

56   therefore has two possible transcriptional states corresponding to one active repressor gene,

57   and the other repressed. Gene networks akin to the toggle switch are thought to help stabilize

58   and refine spatial boundaries within differentiated populations because the two expression

59   states of the toggle are generally mutually exclusive (Briscoe & Small, 2015). Toggle-like

60   regulatory components are found throughout developmental processes, such as in the anterior-

61   posterior development of the *Drosophila* blastoderm (Nasiadka et al., 2002; Struhl, 1989), and in

62   the dorsal-ventral development of the vertebrate neural tube (Alaynick et al., 2011; Dessaud et

63   al., 2008).

64   In multicellular systems, toggle switches can function independently. In the absence of

65   any external signal (e.g., morphogens), the internal stochastic dynamics and bias of each cell

66   determine the transcriptional states of the respective toggle switches. In other words, each cell

67   randomly assumes one of the two states. However, in the presence of an external morphogen

68   gradient, a distinct boundary is formed between cells in the two different transcriptional states.

69   This can occur if the toggle switch exhibits hysteresis (bistability) as a function of the

70   morphogen.

71   Here, we built a version of the genetic toggle switch in *Escherichia coli* that uses

72   intercellular signaling to reinforce each transcriptional state. For instance, if a cell is in the "ON"

73   state it produces an intercellular signal that up-regulates the ON state in nearby cells. The

74   addition of intercellular signaling to the toggle has been proposed as a means of creating a

75   population-level toggle switch, allowing all cells in the population to simultaneously reside in one

76   of the two possible transcriptional states (Nikolaev & Sontag, 2016). We experimentally confirm

77   that, given the right conditions, this version of the toggle does exhibit population-level bistability

78   in a well-mixed liquid culture. Additionally, we show that when grown on solid agar imbued with

79   an exogenous morphogen, colonies of these cells form three dimensional patterns that are

80   distinctly different from those observed in colonies of cells containing a traditional toggle switch

81   lacking intercellular signaling. In particular, the addition of intercellular signaling creates a

82   regime that enables a shift in the resulting pattern. We develop a mechanistic mathematical

83   model of the system, to explain how degradation, diffusion, and sequestration of the signaling

84   molecules and inducers determine the observed patterns.

85

86   **Results**

87   **General characteristics of QS and NQS toggles**

88   Here, we call the version of the toggle switch that includes intercellular signaling the "QS

89   toggle", as it uses refactored **q**uorum **s**ensing pathways to generate intercellular signals. The

90   QS toggle is a version of the genetic toggle switch (Gardner et al., 2000a) that includes two

91   repressors that repress each other's promoters (LacI and TetR). Additionally, it includes a

92   reporter for each state (YFP and CFP). The circuit also includes two orthogonal QS pathways

93   (CinR/I and RhlR/I) (Chen et al., 2015; Lithgow et al., 2000; Pesci et al., 1997) to produce the

94   necessary intercellular signaling. A representation of the QS toggle's two fluorescent states is

95   shown in Fig. 1A. For the yellow state to be active (Fig. 1A, left), LacI represses the promoters

96   driving the expression of *tetR*, *cfp* and *rhlI*. With *tetR* repressed, *cinI* is expressed, and its

97   protein catalyzes the production of C14-HSL. When bound to the CinR transcription factor, C14-

98   HSL activates the expression of *lacI* and *yfp*. Alternatively, for the blue state to be active (Fig.

99   1A, right), TetR represses the promoters driving the expression of *lacI*, *yfp* and *cinI*. With *lacI*

100   repressed, *rhlI* is expressed, and its protein produces C4-HSL. When bound to the RhlR

101   transcription factor, C4-HSL activates the expression of *tetR* and *cfp*. One can exogenously

102   induce the yellow state by adding anhydrotetracycline (aTc), which will inactivate TetR (Fig. 1E).

3

103   Similarly, one can exogenously induce the blue state by adding isopropyl-β-D-1-

104   thiogalactopyranoside (IPTG), inactivating LacI (Fig. 1D). The QS toggle is unbalanced in the

105   absence of inducers: it exhibited a preference to the blue state (Fig. 1D, E). We also found that

106   this imbalance is dependent on the QS network (Fig. S2I, J). The interaction of the main circuit

107   elements is summarized in Fig. 1C. The QS toggle topology (Fig. 1C, left) differs from the

108   conventional (**n**on-**q**uorum **s**ensing toggle or "NQS toggle"- Fig. 1C, right) topology by the

109   presence of two QS networks, creating extra positive feedback loops. The NQS circuit includes

110   the same repressors and reporter genes but driven by promoters that are only responsive to

111   these repressors (Fig. 1B). The NQS toggle can also be tuned with IPTG and aTc (Fig. 1F and

112   1G). For all experiments, we transformed the plasmid-borne QS and NQS circuits into *E. coli*

113   cells that contained constitutively expressed *cinR* and *rhlR* in their genome.

4
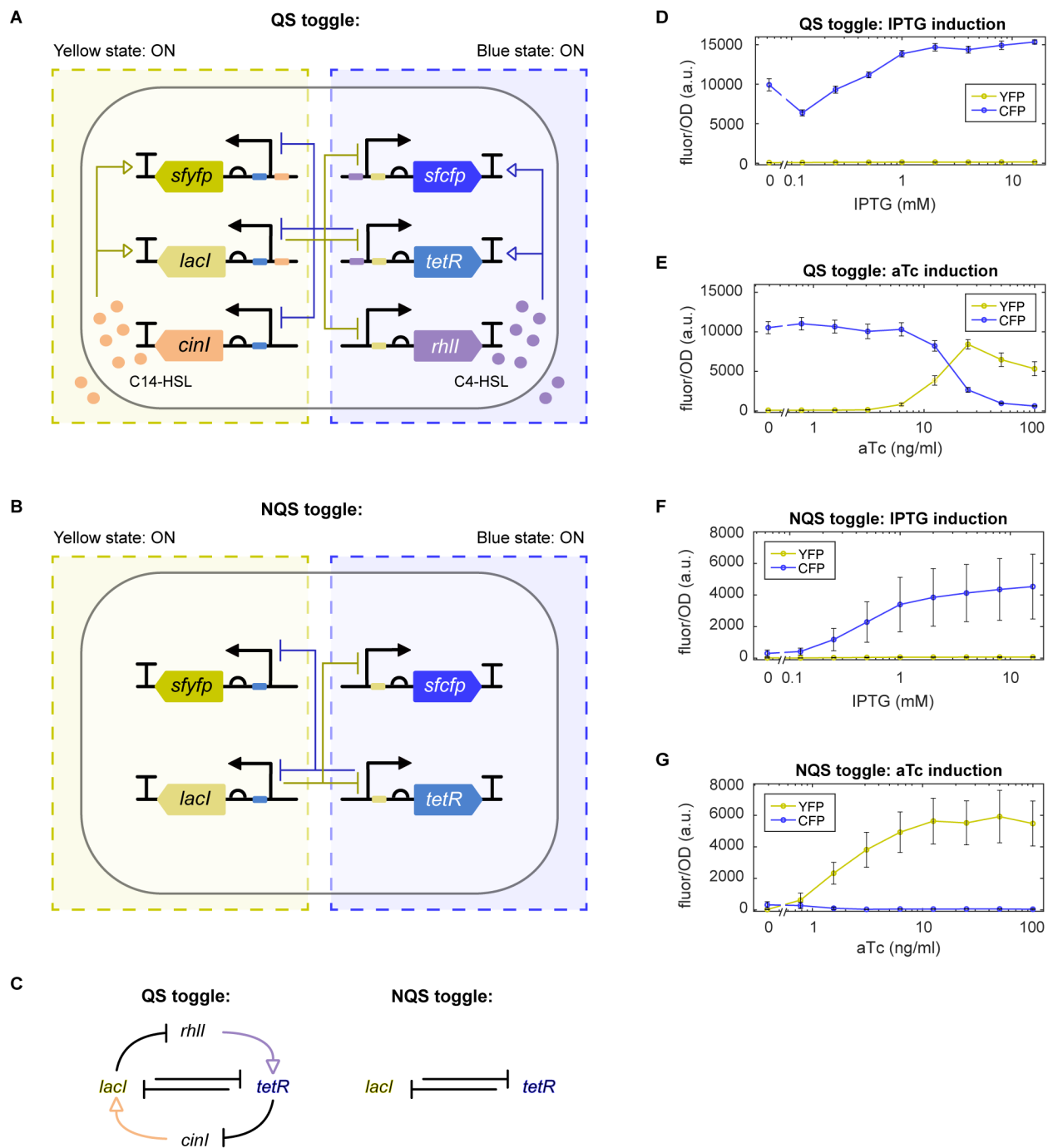
Figure 1: QS and NQS toggle circuit design. For both circuits, IPTG can induce the blue state, while aTc can induce the yellow. **A)** QS toggle: When the yellow state is ON, LacI represses *tetR*, *rhlI* and *sfcfp* genes, while C14-HSL activates *lacI* and *sfyfp* genes. When the blue state is ON, TetR represses *lacI*, *cinI* and *sfyfp* genes, while C4-HSL activates *tetR* and *sfcfp* genes. **B)** NQS toggle: When the yellow state is ON, LacI represses *tetR*, and *sfcfp* genes. When the blue state is ON, TetR represses *lacI* and *sfyfp* genes. **C)** The QS and NQS toggle topologies differ by the presence of 2 QS networks. **D)** QS toggle induction with IPTG in liquid culture. **E)** QS toggle induction with aTc in liquid culture. **F)** NQS toggle induction with IPTG in liquid culture. **G)** NQS toggle induction with aTc in liquid

5

122 culture. Lines represent the average fluorescence and error bars represent the standard deviation of 3 technical

123 replicates for 3 independent experiments.

124

125   We first checked whether cells containing the QS toggle exhibited population-level

126 bistability. Genetic toggles are often bistable (Barbier et al., 2020; Gardner et al., 2000a;

127 Lugagne et al., 2017; Wang et al., 2009), *i.e.* they can stably reside in either of two possible

128 transcriptional states. To find the bistable region for both the QS and NQS toggles, we grew

129 overnight cultures with either IPTG or aTc to allow for the populations to start in either state

130 (blue or yellow, respectively). We then grew these cells in liquid culture using various

131 combinations of IPTG and aTc concentrations and used flow cytometry to measure the CFP and

132 YFP fluorescence of individual cells. After three hours, we observed that, when starting in the

133 yellow state (*i.e.* previously grown in media with aTc), QS toggle cells all remained in the yellow

134 state for all combinations of inducer (Fig. 2A, right). However, when starting in the blue state

135 (i.e., previously grown in media with IPTG), QS toggle populations shifted to the yellow state at

136 sufficiently high aTc but remained in the blue state at lower concentrations (Fig. 2A, left).

137 Importantly, we observed cultures in which all cells were either in the blue or yellow state

138 depending on the starting condition and the inducer concentration (Fig. 2A) – indicating that the

139 QS toggle is bistable at the population level in those conditions. Meanwhile, NQS toggle cells

140 transitioned to blue and yellow, when starting from the opposite color initial conditions (Fig. 2B).

141 We also observed that cells pre-induced with IPTG primarily did not show any fluorescence (Fig.

142 2B, left), although the blue state was inducible. A third state (OFF), in which cells exhibited little

143 to no fluorescence of either type, was more common within NQS cells. The NQS toggle was

144 also bistable for some conditions. When growing the cells for 9 hours instead, the NQS toggle

145 showed a decrease in both intensities in all tested conditions, while the QS toggle tended to

146 show stronger fluorescence intensities (Fig. S1).

147

6

148
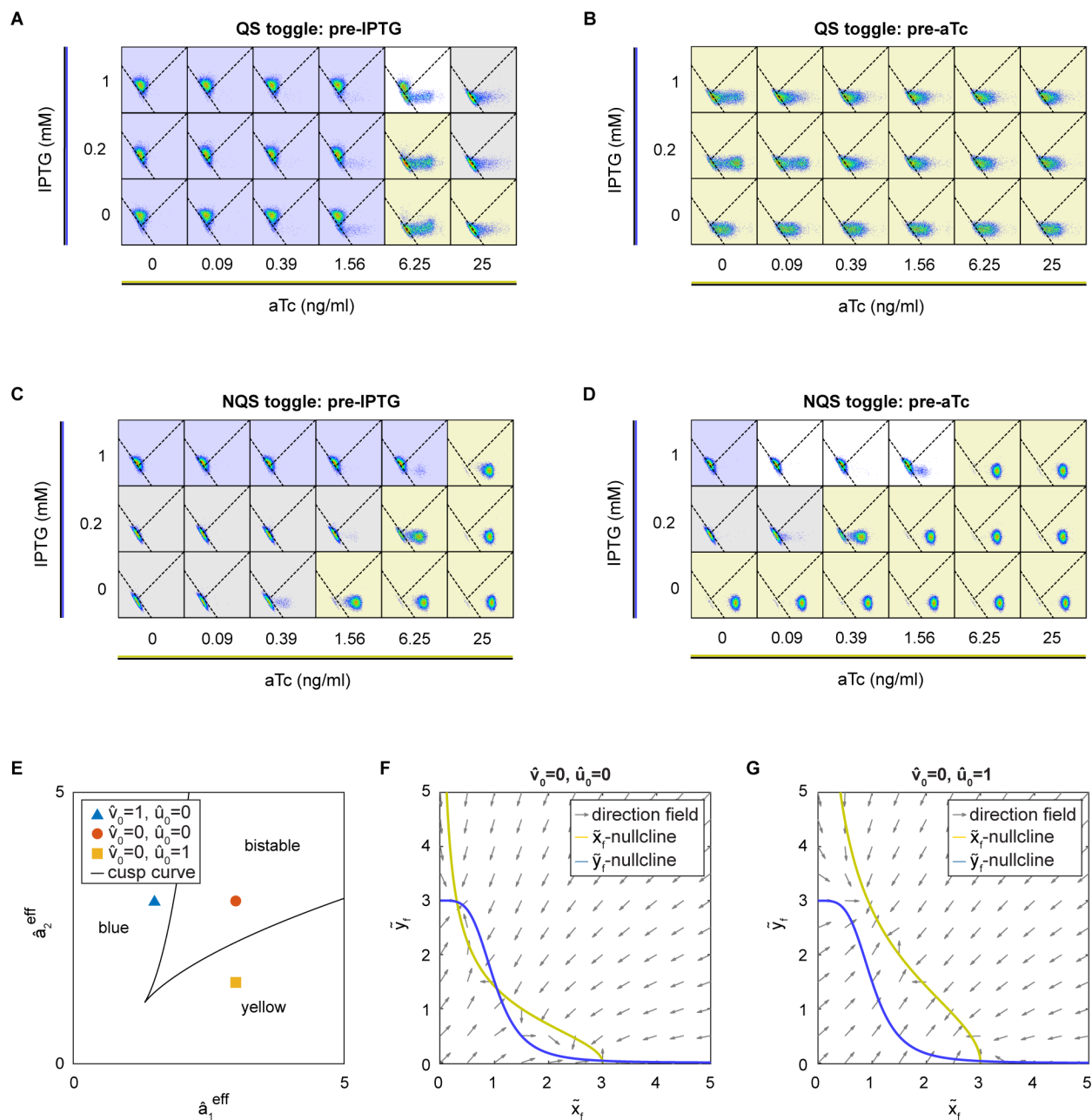
Figure 2: Behavior of QS and NQS toggle cells when treated with a combination of inducers. A-B) Flow cytometry data of QS toggle cells that were pre-induced with either IPTG (A) or aTc (B). Each dot is a single cell classified within a gate. Gates were determined with single color and double negative controls. Dashed lines in each plot represent the boundaries between the three distinct gates, which represent cellular states: CFP+ (top gate), YFP+ (bottom-right gate), and OFF (bottom-left gate). Background colors in each plot represent which state the majority of cells are in (>50%): blue color indicates mostly CFP+ cells, yellow plots are mostly YFP+, gray plots are mostly OFF, and white plots indicate cells that are present in multiple states (<50% each). **C, D)** Flow cytometry data of NQS toggle cells that were pre-induced with either IPTG (C) or aTc (D). **E)** Bifurcation diagram of the QS toggle system over the nondimensionalized parameters $\hat{a}_1^{\text{eff}}$ and $\hat{a}_2^{\text{eff}}$, the effective promoter strength of the repressors. Here we demonstrate a case where without exogenous inducers, aTc or IPTG, the system is bistable (red dot). Adding aTc

7

159 or IPTG (blue triangle and yellow square respectively), lowers the effective promoter strength, which can in turn lead

160 to changes in the state of the cell to be monostable in either the blue or yellow state. **F, G)** Phase portrait of the QS

161 toggle system for chosen parameter values denoted by the red dot and blue triangle in E. Variable and parameters in

162 E-G are nondimensionalized (see STAR methods).

163

164   We next developed a mathematical model of the toggle switches to understand under

165 what conditions the two versions of the circuit can exhibit bistability. Denoting by $x(t)$ and $y(t)$

166 the concentration of LacI and TetR, respectively, and by $g(t)$ and $h(t)$ the intracellular

167 concentration of QS signals, C14-HSL and C4-HSL, the model takes the form

168
$$\dot{x} = a_1\eta_1(y)\phi_1(g) - (\gamma_1 + \gamma_d)x; \tag{1a}$$

169
$$\dot{y} = a_2\eta_2(x)\phi_2(h) - (\gamma_2 + \gamma_d)x, \tag{1b}$$

170 where the parameter a_i determines the maximal production rates, γ_i the individual degradation

171 rates for LacI and TetR (numbered $i = 1,2$, respectively), and γ_d the rate of dilution due to cell

172 growth. We model repression and activation of the promoters using Hill functions, η_i and

173 ϕ_i, respectively. The intracellular concentration of QS signals obeys similar equations (See

174 STAR methods for the full model).

175   We nondimensionalized Eq. (1) and performed a bifurcation analysis (see STAR

176 methods), to first confirm the existence of the region of bistability in the QS toggle system model

177 (See Fig. 2E). Moreover, as is evident in the production term of LacI and TetR in Eq. (1), the

178 preferred state of the QS toggle is not determined only by the presence of the QS signals, but

179 also the relative promoter strength. This is characterized by the following nondimensionalized

180 variables,

186
$$\tilde{a}_1 = \frac{a_1\theta_x}{\gamma_1 + \gamma_d} \text{ and } \tilde{a}_2 = \frac{a_2\theta_y}{\gamma_2 + \gamma_d}, \tag{2}$$

181 where θ_x and θ_y are the repression thresholds for LacI and TetR, respectively, used in the Hill

182 functions, η_i. When exogenous inducers, aTc or IPTG, are added to the system, the relative

183 promoter strength is modified. Following experiments, we assumed that these inducers are

184 provided at some constant level, denoted by nondimensionalized parameter $\hat{v}_0$ and $\hat{u}_0$. This

185 leads to the following effective promoter strengths,

187
$$\hat{a}_1^{\text{eff}} = \frac{\tilde{a}_1}{1 + \hat{v}_0}\frac{\tilde{g}^*}{1 + \tilde{g}^*}, \qquad \hat{a}_2^{\text{eff}} = \frac{\tilde{a}_2}{1 + \hat{u}_0}\frac{\tilde{h}^*}{1 + \tilde{h}^*}, \tag{3}$$

188 with $\tilde{g}^*$ and $\tilde{h}^*$ representing the nondimensionalized C14 and C4 concentrations in the system.

189 Depending on the values of the bifurcation parameters $\left(\hat{a}_1^{\text{eff}}, \hat{a}_2^{\text{eff}}\right)$ the system can be either

190 mono- or bistable (see Fig. 2E-G; STAR methods for the full model).

8

191   The mathematical model thus predicted that bistability depends on the QS network and
192   relative promoter strengths. We tested this prediction experimentally by engineering a few
193   variants of the QS toggle that changed those factors (see SI). These variants exhibited changes
194   in state preference, agreeing with the prediction of the model (Fig. S2).
195
196   **QS and NQS toggle behavior in colonies**
197   We next asked how the QS toggle behaves in an environment in which the QS signals are not
198   homogeneously distributed in the population, allowing for spatial patterns to arise. To do this,
199   we grew QS and NQS toggle colonies in LB agar plates containing aTc and monitored their
200   growth and fluorescence over time.
201   Most strikingly, we noticed that many QS toggle colonies formed a blue ring surrounding
202   a yellow disc (Fig. 3A), with the size of the yellow disc correlated with the aTc concentration in
203   the agar (Fig. 3B). ATc is known to be temperature sensitive (Politi et al., 2014). Since aTc
204   induces the expression of the yellow state, we hypothesized that aTc degradation was driving
205   the emergence of blue cells. Indeed, we verified that prior incubation of aTc plates at 37ºC
206   directly alters the blue ring size and time of appearance (Fig. S3). Thus, the decay of aTc
207   creates a temporal morphogen gradient, resulting in a switch in the state of some of the
208   population.

9
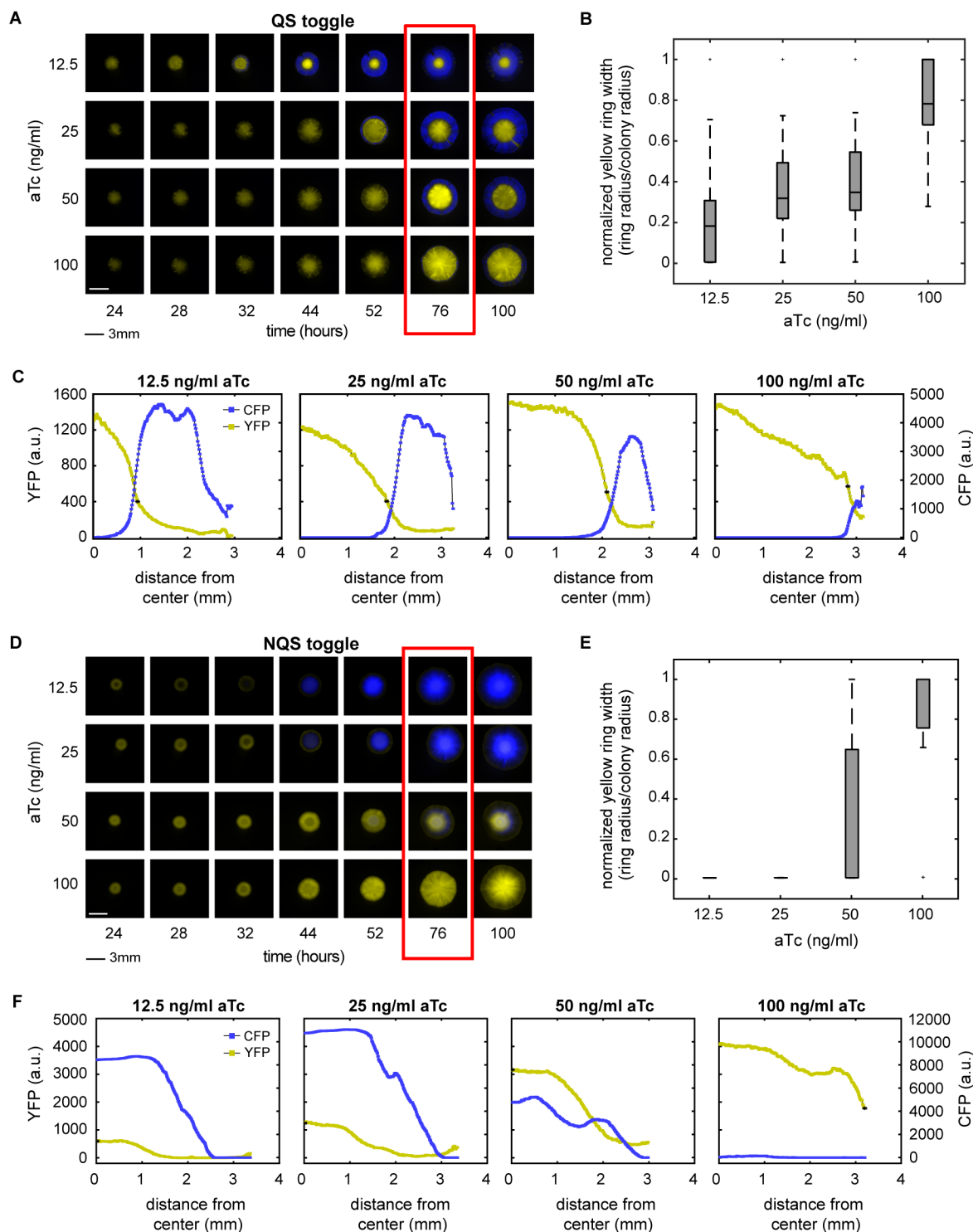
Figure 3: Expanding QS and NQS toggle colonies show aTc-dependent patterning. A) QS toggle colonies obtained from plates with different initial aTc concentrations, shown at different times. **B)** Yellow ring width (center disc) was measured among all colonies to quantify the pattern. The width was determined as the distance from the center to the threshold point, at which yellow fluorescence fell below 30% of its maximum. The only pairwise combination of widths not found to be statistically different was 25 and 50 ng/ml aTc ($p < 0.01$, Kruskal-Wallis non-

10

215 parametric test). Data represents at least 11 independent experiments. **C)** Fluorescence intensity cross-sectionals of
216 the colonies shown in red in (A). Curves represent the average fluorescence of 4 radii (90° apart) of the same colony.
217 **D)** NQS toggle colonies obtained from plates with different initial aTc concentrations, shown at different times. **E)**
218 Yellow ring width was used to quantify the patterns as in (B). We considered yellow ring width to be zero when blue
219 cells dominate the center (see methods for full set of assumptions). All pairwise that included 100 ng/ml aTc were
220 found to be statistically different (*$p < 0.01$, Kruskal-Wallis non-parametric test). Data represents 2 independent
221 experiments. **F)** Fluorescence intensity cross-sectionals of colonies shown in red in (C). Curves represent the
222 average fluorescence of 4 radii of the same colony.

223

224   In the images of QS toggle colonies, we observed little overlap between cells in the
225 yellow and blue states (Fig. 3C). Over time, the blue ring generally expanded as the colony
226 grew, but the boundary between the yellow and blue cells remained roughly fixed. Wherever
227 cells in the blue state took over, yellow fluorescence tended to decrease.
228   When grown on solid media, the NQS toggle behaved differently from the QS toggle.
229 Like the QS toggle, NQS toggle colonies were initially yellow when the media contained a high
230 enough concentration of aTc. Cells in the blue state emerged eventually but did so in a way
231 distinct from what we observed in the QS toggle: Blue cells first appeared in colony centers, and
232 did so earlier and at lower aTc concentrations (Fig. 3D). Most NQS toggle colonies grown with
233 12.5-50 ng/ml aTc showed blue cells in the center at 76h (Fig. 3E), which resulted in yellow
234 region width measurements close to zero (see Methods).
235   One of the main differences in spatial patterns between the two toggles was the degree
236 of radial separation between the states. The QS toggle colonies appeared to segregate well in
237 contrast to the NQS toggle colonies (Fig. 3F). To quantify the level of segregation, we measured
238 the pixel color overlap in images from both QS and NQS colonies: For each pixel, we measured
239 the intensity of both blue and yellow fluorescence and in Fig. 4A and B (bottom panels), we
240 show the normalized YFP and CFP fluorescence as a function of distance from the center of the
241 colony. We said that colors overlapped in a pixel when the values of both YFP and CFP
242 fluorescence intensities were each above a threshold of 0.3 (out of a maximum intensity
243 normalized to 1). To obtain the relative overlap count for a colony, we divided the number of
244 overlapping pixels by the total number of pixels covering the colony radius (See Fig. 4C).
245   Color overlap was significantly higher in the NQS compared to QS colonies in 12.5, 25,
246 and 50 ng/ml aTc plates ($p < 0.01$, Mann-Whitney non-parametric test). In 100 ng/ml aTc plates,
247 we observed little overlap with both circuits, mostly because not all colonies contained cells in
248 the blue state. When we excluded from analysis colonies with cells in only one state, NQS
249 colonies displayed higher overlap than QS colonies at all aTc concentrations (Fig. S4).
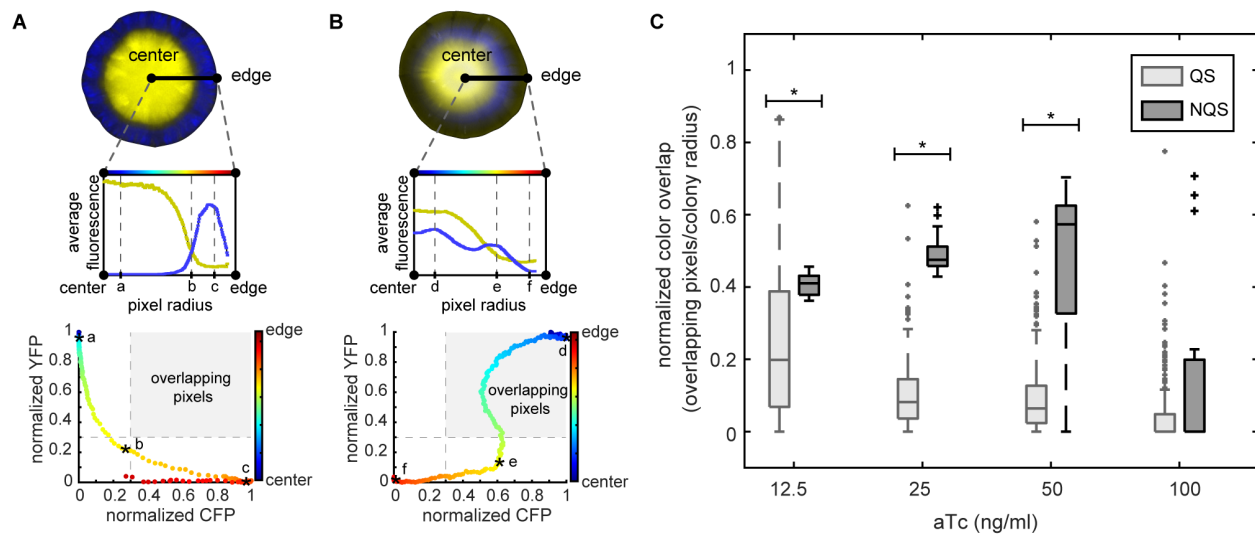
11

Figure 4: QS colonies create better radially separated patterns than NQS colonies. Measurement of color
overlap was used to quantify the spatial segregation of states in each colony. Average fluorescence of each colony's
radii plotted from the center of the colony to the edge (A and B, top plots). Each pixel was also plotted for both
normalized fluorescence values (A and B, bottom dot plots). Pixels were classified as overlapping when both
normalized fluorescence values were above a predefined threshold (inside the gray boxed region). **A)** Example of the
typical behavior of QS colonies. The QS colony shown is the same as that in Fig. 3A, at 50 ng/ml and 76 hours.
Asterisks (a, b, c) show the same pixels in both plots. **B)** Example for the typical behavior in NQS colonies. NQS
colony shown is from Fig. 3C, 50 ng/ml at 76 hours. Asterisks (d, e, f) show the same pixels in both plots. **C)**
Quantification of pixel overlap for QS (light gray) and NQS (dark gray) colonies. The number of overlapping pixels
was normalized by the colony radius (total). *$p < 0.01$, Mann-Whitney non-parametric test. Data for each QS test
contains over 180 colonies from at least 11 independent experiments, while data for each NQS test contains at least
15 colonies from 2 independent experiments.

Lower overlap indicates a better separation of colors, and hence a better spatial
separation of cells in the two states along the radial direction of a colony. Therefore, QS cells in
different states were better segregated radially than NQS cells. However, since we imaged the
colony from above, the higher degree of overlap in the NQS case could indicate either that cells
in the two states are intermingled, or that they are segregated vertically. To test which of these
hypotheses is more likely, we extended our mathematical models to include spatial effects, such
as colony growth, and the diffusion of inducers and signaling molecules within the agar and the
colony. We assumed that the colony is conical and grows through the addition of cells in an
active growing zone at the interface of the colony with agar (Warren et al., 2019) (see STAR
methods).

Simulations of our expanded models recapitulated experimental observations, and
suggested answers to our questions about the observed segregation of cells in different states.

12

276   In the simulations of the NQS toggle colony (Movie S1), with smaller colony sizes and abundant

277   aTc supply from the agar, aTc levels are relatively high everywhere in the NQS toggle colony.

278   This explains the initial colony-wide yellow state we observed in experiments (Fig. 3D). In this

279   initial yellow state, intracellular concentration of TetR is low, leading to a low sequestration rate

280   of aTc inside the colony. The top of the colony is further from the aTc source (agar), so that a

281   top-down aTc gradient forms over time. As the model colony grows, we observe an increase in

282   sequestration and degradation of aTc (due to 37ºC incubation over time). Eventually, the aTc

283   level at the top of the colony, where concentration is lowest, degrades below the point needed

284   to keep cells in the yellow state, causing the top of the colony to turn blue. Cells entering the

285   blue state produce more TetR, which enables higher aTc sequestration, further lowering

286   surrounding aTc levels. As a result, we observed a blue wave traveling downwards from the top

287   of the colony. Thus, our model predicted that the two states are vertically segregated in NQS

288   colonies, suggesting that spatial segregation, rather than heterogeneity, is responsible for the

289   experimentally observed color overlap. We also examined the state of the system by tracking

290   the bifurcation parameters (Eq. 3) at the center (top) and the periphery (rim) of the NQS colony

291   over time (Fig. 5D). In simulations, the top of the colony moves from the bistable state into the

292   blue state, while the rim of the colony remains in the yellow state (Fig. 5B, C). Our simulations

293   and bifurcation analysis also revealed that at higher initial aTc concentrations the blue state

294   takes over from the top at a later time (Fig. 5A), as it takes longer for aTc to degrade to the

295   hysteresis point at which cells can switch states.

13
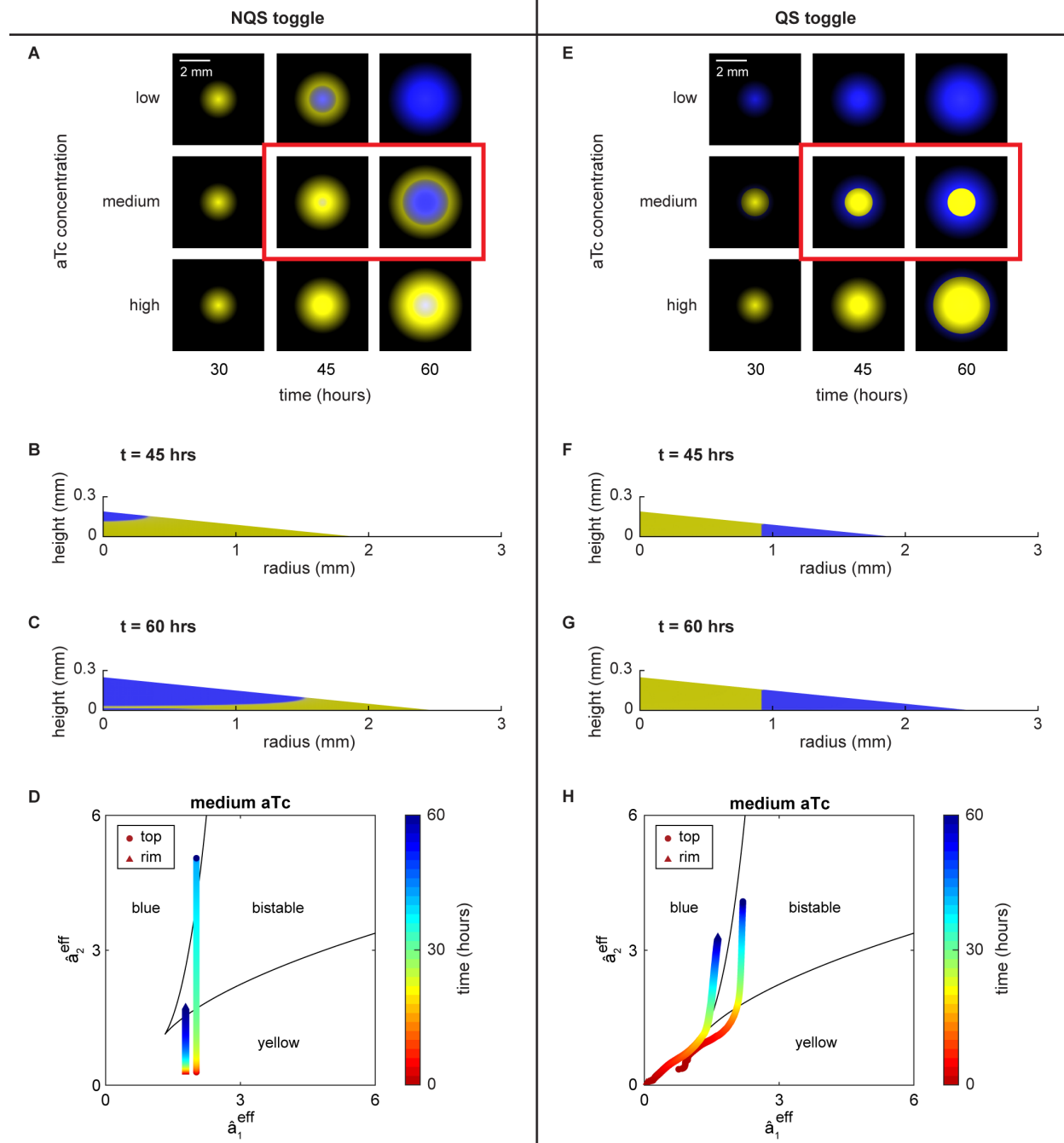
Figure 5: PDE simulations of NQS and QS toggles. A) Simulations of the NQS colony at different times and initial aTc concentration show the emergence of cells in the blue cells at the center of the colony. **B)** The cross-sectional view of the model colonies shows that cells enter the blue state first at the top of the colony, and that cells in the two states remain vertically segregated. **C)** Bifurcation diagram showing the bifurcation parameters' trajectories of cells at the top (circle) and rim (triangle) of the NQS colony. The top of the colony flips from yellow to blue. **D)** Simulations of a model QS colony show that a blue ring emerges dependent on the initial aTc concentration. **E)** The cross-sectional view of the model colonies shows that the cells in the two states are radially segregated, and that the boundary between the two states is roughly fixed, in agreement with experiments. **F)** Same as in C), but showing that in the QS colony the rim of the colony flips from the yellow to blue state.

14

306

307   In simulated QS toggle colonies (Movie S2), when the colony is small, abundant aTc and

308 basal C14-HSL production led to the establishment of the initial yellow state across the colony.

309 This state was then reinforced by the high C14-HSL signal. As indicated by Eq. 2, the dilution

310 rate alters the effective promoter strength, leading to different steady states. Cells that are not

311 growing or growing slowly, such as those at the top of the colony, stay in the bistable region,

312 and do not switch states (Fig. 5H). This explains why the center of the colony remains yellow,

313 despite reduced aTc levels due to degradation and sequestration. In contrast, for fast-growing

314 cells, the drop in aTc concentration and the slow accumulation of C4-HSL signal from basal

315 production allow cells to enter the blue state (Fig. 5F). Cells in the blue state start to appear at

316 the periphery of the colony, where cells grow fastest (Movie S2). This explains why in the QS

317 toggle color overlap is small (vertical slices are in the same state), and the boundary between

318 the yellow and blue states is maintained at the point where the first cells turn blue (Fig. 5F, G),

319 in agreement with experimental observations (Fig. 3A). Like the NQS toggle, higher aTc

320 concentrations lead to the blue ring emerging later in time (Fig. 5E).

321   To verify the predictions of the model about the different spatial structures in QS and

322 NQS colonies, we used confocal microscopy to image the 3D structures of the colonies (Fig. 6).

323 For the NQS toggle, we observed that the colonies indeed showed vertical segregation, with

324 cells at the top of the colony dome in the blue, and cells at the bottom in the yellow state (Fig.

325 6C, F). We also sliced the colonies vertically and imaged their cross-sections using confocal

326 microscopy (see Methods). The slices confirmed that cells in the blue state occupied the top of

327 NQS colonies, while cells in the yellow state occupied the bottom, as predicted by the model

328 (Fig. 6F). In contrast, confocal images of QS toggle colonies displayed radial separation

329 between the states, again confirming the predictions of the model, and in agreement with our

330 earlier analysis of experimental findings (Fig. 6A, E). Depending on the aTc concentration, the

331 QS toggle cells at the top of the colony remained yellow, and blue cells only appeared in the

332 outer part of the colony. Imaging of colony slices also confirmed this observation (Fig. 6E).

15
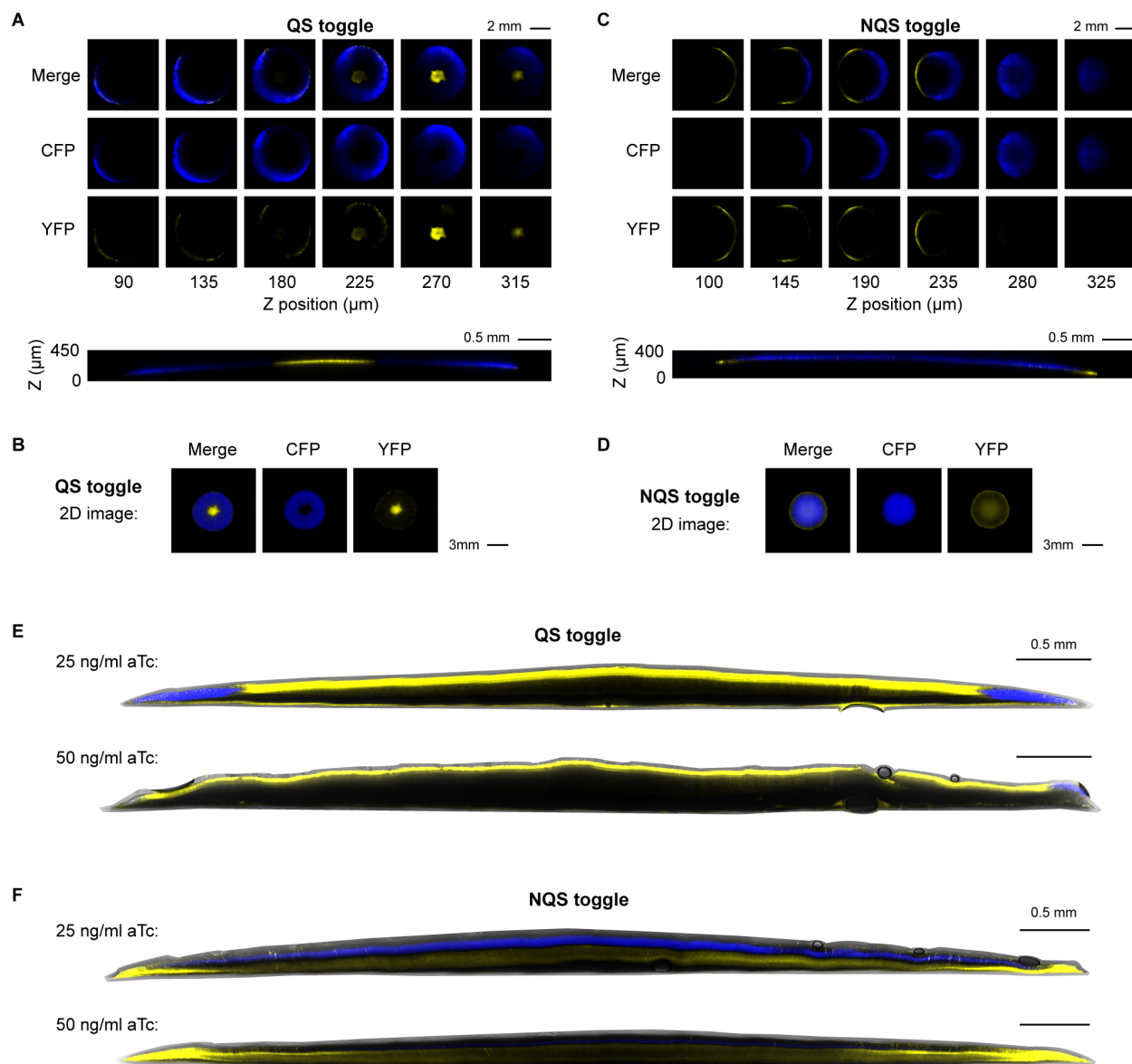
Figure 6: Three-dimensional view of QS and NQS colonies. A) QS toggle layers from top to bottom of colony (left to right). Orthogonal view of the QS toggle frames is shown below. Colony is not more than 250 μm tall. **B)** 2D image of the same colony in (A) for comparison. Separate fluorescence channels are shown. **C)** NQS toggle layers from top to bottom of colony (left to right). Orthogonal view of the NQS toggle frames is shown below. **D)** 2D image of the same colony in (C) for comparison. Separate fluorescence channels are shown. **E)** Slices of different QS colonies grown in either 25 or 50 ng/ml aTc. **F)** Slices of different NQS colonies grown in either 25 or 50 ng/ml aTc.

We found that ring formation in the QS toggle exhibited some variability and randomness causing imperfect radial symmetry of the outer blue rings. Despite this variability, the difference in color segregation between QS and NQS colonies was statistically significant (see Fig. 4). Occasionally, we also observed the occurrence of multiple blue rings: *i.e.* the formation of internal and external blue rings in QS toggle colonies (Fig. 7 and S5). In addition, patches of

16

346   blue cells sometimes failed to form a full ring (Fig. S5). These observations suggested that

347   external or internal fluctuations could play a role in determining the observed spatial patterns.

348   Noise can cause jumps between the stable states of a bistable system. However, we expect

349   such switches to be localized in the absence of a mechanism that can synchronize the state

350   across the colony. Thus, we concluded that external fluctuations that affect all or most of the

351   colony were more likely to drive the emergence of complex spatial patterns such as multiple

352   rings. Furthermore, when the QS toggle was grown in a different medium (EZ rich defined

353   medium instead of LB agar), the outer blue ring pattern was disrupted. At times, we observed

354   blue cells emerging from the center of the colony at 100 ng/ml aTc. These patterns resembled

355   those in the NQS toggle in LB agar (Fig. 7 and S6).
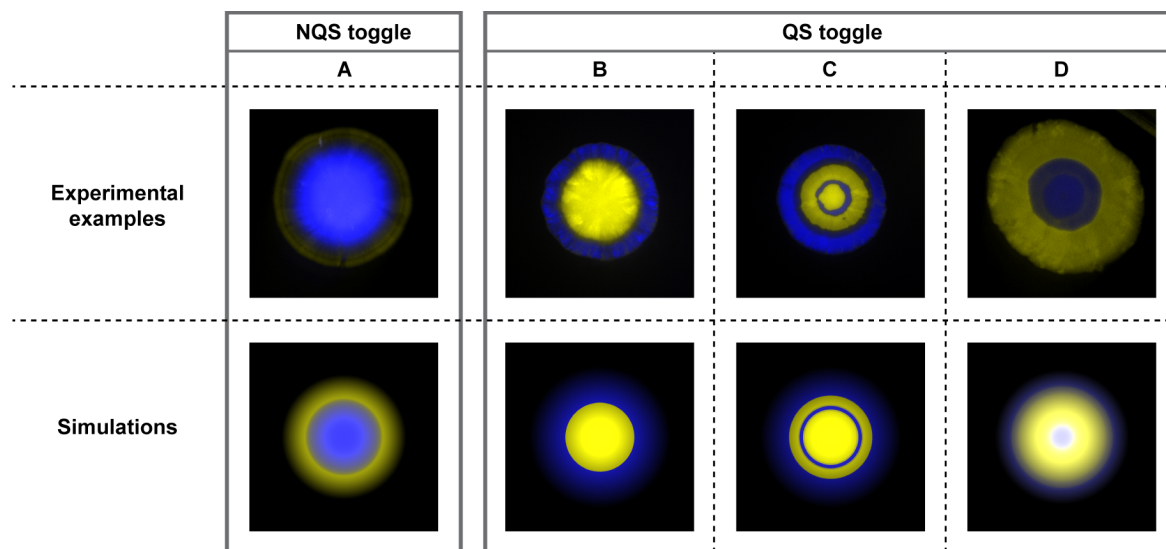
356
357   **Figure 7: Four types of patterns obtained from experiments (top) and mathematical simulations (bottom). A)**
358   NQS toggle colony pattern, with vertical segregation of states and blue emergence at the center of the colony. **B)** QS
359   toggle colony pattern, with radial segregation of states, and blue emergence at the edge of the colony, forming an
360   external blue ring. **C)** Alternative QS toggle pattern, with radial segregation of states and multiple blue rings (internal
361   and external). **D)** Inverted QS toggle pattern, where radial segregation of states and blue emergence at the center
362   occur only in specific conditions (see SI).

363

364   We were able to obtain similar patterns in numerical simulations by changing parameter

365   values, or by including extrinsic perturbations in the model we described above (Fig. 7 and

366   STAR methods). In particular, we found that extrinsic fluctuations and growth conditions can

367   change effective promoter strength, resulting in the formation of multiple rings and an inverted

368   pattern in the QS system, respectively. This suggests that the complex spatial patterns we

369   observed in some experiments can be explained using the same mechanisms underlying the

370   predominant, single ring patterns. The variability of multi-ring patterns, along with the high

17

371   dimensionality of the model parameter space makes it difficult to examine such patterns

372   systematically. A full understanding of how these complex patterns emerge, and how they can

373   be controlled will thus require the development of new experimental approaches.

374

375   **Discussion**

376   Patterns, and especially ring-like patterns, formed by synthetic gene circuits are not new.

377   Previous studies have utilized various methods to create patterns, such as internal genetic

378   oscillations (Riglar et al., 2019), scale-invariant intracellular signaling (Cao et al., 2016), or

379   mechanical interactions between cell types (Xiong et al., 2020). Here we show that toggle

380   switches can also create patterns in colonies based on how they shape the cells' responses to a

381   morphogen. Specifically, the classical NQS toggle creates a vertically segregated pattern while

382   the QS toggle leads to a segregated ring structure. We also developed a PDE model that

383   captured both behaviors. An analysis of the model suggests that in the NQS case sequestration

384   of signals and geometry of the colony lead to the formation of a morphogen gradient inside the

385   colony, creating top-down segregation. In contrast, the model suggests that fast cell growth at

386   the periphery of QS toggle colonies and the QS signal gradient inside the colonies lead to the

387   emergence of an outer blue ring. The difference is that, as the aTc level decreases in the QS

388   toggle, signaling between cells in the yellow core helps to lock them in the same state.

389   However, in the NQS toggle, the blue state becomes monostable in the absence of aTc and

390   signals from other cells. As the aTc concentration is lowest at the top of the colony, a wave of

391   transitions from the yellow to the blue state propagates from the colony's top downward. Our

392   mathematical analysis implies bistability is determined by the external morphogen concentration

393   and the effective promoter strength for each repressor, which is, in turn, determined by protein

394   production, proteolytic degradation, dilution, and QS signals.

395   Our mathematical model provides further insight into the mechanisms behind the

396   formation of patterns. When modeling pattern formation on the time scale of hours, one must

397   account for expanding colony size. As suggested by Warren et al. (2019), an actively growing

398   layer at the bottom of the colony drives the 'establishment phase' (14h – 24h). After 24 hours,

399   the colony enters a 'flattening phase', during which vertical growth slows while radial growth

400   remains linear. In our model, the characteristic length scale of signal diffusion is much larger

401   than the size of a colony, and thus details of the colony expansion mechanisms do not have a

402   large impact. We thus assumed that model colonies grow linearly in both vertical and radial

403   directions. The location of newly born cells, on the other hand, does matter. As new cells inherit

18

404 the state of their parent cells, where the effective promoter strengths of the newly born cells land
405 in the bistable region determines the emergent patterns in the colony.

406 It should be noted that our model does not precisely predict the full behaviors of the
407 colonies. Our experiments showed that fluorescence intensities were lower in the bulk of many
408 colonies and higher nearer the surface (Fig. 6E). This indicates that the colonies are more
409 complex than our model suggests. Yet, our model still provides qualitative insight into the
410 formation of the patterns and their symmetries. Further experimental studies on *E. coli* colony
411 growth, structure, and metabolism, especially at larger colony sizes, will allow for improvement
412 of the mathematical model and a better understanding of pattern formation in microbial colonies.

413 Our work indicates that the observed spatial patterns are dependent not just on the
414 underlying genetic circuitry, but also on growth conditions and cellular metabolism. Our
415 mathematical model allows us to identify which patterns are allowed by the system and the
416 mechanisms that generate them. The presence or absence of intercellular communication, for
417 instance, is not the determinant of a single pattern. Rather, the resultant pattern is determined
418 by multiple factors, including morphogen concentration, promoter strengths, and intercellular
419 signaling. Nevertheless, the presence of intercellular signaling allows one to actively control or
420 shape the balance by implementing more spatial features, such as signal degradation, by
421 differentiated cells or external flux. These patterns shed light into how synthetic multicellularity
422 can be created in bacteria and provide a further step toward the creation of large scale
423 programmable synthetic multicellular systems.

424

425 **Acknowledgements**

435

436 **Author contributions**

19

437   Conceptualization, B.F.M., G.F., E.D.S., K.J., M.R.B.; methodology, B.F.M., G.F., E.D.S., K.J.,

438   M.R.B; validation, B.F.M., M.R.B.; data curation, B.F.M.; investigation, B.F.M., G.F.; formal

439   analysis, B.F.M., G.F; visualization, B.F.M., G.F.; writing – original draft, B.F.M., G.F., K.J.,

440   M.R.B.; writing – review & editing, B.F.M., G.F., E.D.S., K.J., M.R.B.; software, G.F.; project

441   administration, B.F.M., G.F., K.J., M.R.B.; funding acquisition, B.F.M., K.J., M.R.B.; supervision,

442   K.J., M.R.B.

443

444   **Declaration of interests**

445   The authors declare no competing interests.

446

447   **Main figure titles and legends**

448   (In text)

449

450   **STAR Methods**

451   **Methods**

452   **Plasmids and strains**

453   We constructed plasmids with either PCR-based, restriction enzyme cloning, or Golden gate

454   assembly methods. QS and NQS toggles, as well as all other tested versions, are composed

455   with 3 plasmids each, providing resistance to kanamycin, chloramphenicol and spectinomycin. A

456   list of all plasmids employed is provided in Table S1. For this study, we used the CY027 *E. coli*

457   strain, a BW25113 derivative (Chen et al., 2015). This strain has the *lacI*, *araC* and *sdiA* genes

458   knocked out, and constitutive *cinR* and *rhlR* knocked-in to its genome to enable QS

459   communication (*ΔlacI ΔaraC ΔsdiA Ptrc*-cinR Ptrc*-rhlR*).

460

461   **Plate reader experiments**

462   From single colonies, we inoculated cells containing the appropriate plasmids into 5 mL LB with

463   antibiotics (50 μg/mL kanamycin, 34 μg/mL chloramphenicol, 50 μg/mL spectinomycin) for

464   overnight growth at 37°C in a shaker (250 rpm). Then, we diluted the culture 1:100 in minimal

465   M9CA broth (Teknova) with antibiotics, and we grew these cells for 2 hours in a 37°C shaker

466   (250 rpm). Meanwhile, we prepared 96-well round bottom plates with minimal M9CA broth,

467   antibiotics, and applicable inducers (IPTG and aTc) with a 2-fold final concentration of a volume

468   of 100 μL per well. After the 2-hour growth, we added 100 μL of cell outgrowth to each well

469   (1:1). We incubated the plates at 37°C, shaking at 800 rpm. After 2 hours, we read each plate in

470   a Tecan Infinite M1000 for growth (OD, 600 nm), YFP fluorescence (ex, 514 nm; em, 527 nm),

20

471   and CFP fluorescence (ex, 433 nm; em, 475 nm). We used cells without plasmids to measure

472   background auto-fluorescence. The results shown are reported as (fluorescence-

473   background)/OD$_{600}$.

474

Flow cytometry

476   We inoculated cells from single colonies into 5 mL LB with antibiotics and either 0.5 mM IPTG

477   (pre-IPTG) or 50 ng/ml aTc (pre-aTc) for the overnight growth at 37°C in a shaker (250 rpm).

478   Next, we prepared 96-well round bottom plates with minimal M9CA broth, antibiotics, and

479   applicable inducers (IPTG and aTc) with a 2-fold final concentration at a volume of 100 μL per

480   well. We diluted the overnight cultures 1:50 in minimal M9CA broth with antibiotics, and we

481   added 100 μL of this cell dilution to each well (1:1, final cell dilution of 1:100). We incubated the

482   plates at 37°C, shaking at 650 rpm. After 3 hours (and 9 or 12 hours for stationary phase tests),

483   we kept the plates on ice for at least 10 min. Then, we added 25 μL of each well to a tube with

484   475 μL of 1x PBS (5% dilution), and vortexed the tube. We analyzed each tube with the Sony

485   SH800S Cell Sorter. We used filters for mCFP and EYFP. Due to overlap in their fluorescence

486   spectra, we used single fluorescence controls and the Sony software calculated compensations

487   for each fluorophore. All CFP and YFP values shown here are compensated. For each sample,

488   we recorded 10,000 events. We exported and analyzed the acquired data with FlowJo. We

489   manually created the fluorescence gates. The common existence of OFF cells among the

490   circuits (i.e., cells that are expressing neither CFP nor YFP) generated the need for an OFF

491   gate. We created blank controls for each circuit by transforming the circuit plasmids with an

492   empty reporter plasmid instead of the regular CFP/YFP one. We used these circuits to

493   determine the OFF gate. Next, we created CFP+ and YFP+ gates by drawing a diagonal line

494   from top right to bottom left, until it reaches the OFF gate. CFP+ gate is at the upper left of this

495   line, while YFP+ is at the bottom right. We exported geometric mean values and population

496   composition based on these gates from FlowJo and plotted with Matlab. For the confocal tests,

497   we also used the Sony SH800S to sort single cells into small petri dishes (60 mm) containing LB

498   agar. We attached the dishes to the 96-well-plate stage for sorting, and later put them into 37°C

499   incubator for growth into single colonies.

500

Colony tests

502   We prepared LB agar plates with antibiotics (50 μg/mL kanamycin, 34 μg/mL chloramphenicol,

503   50 μg/mL spectinomycin), and aTc (12.5, 25, 50 or 100 ng/ml). We inoculated cells from single

504   colonies into 5 mL LB with antibiotics and 0.0625 mM IPTG for overnight growth at 37°C in a

21

505   shaker (250 rpm). Next, we diluted the culture 1:100 in 4 mL LB with antibiotics and 0.0625 mM

506   IPTG, and we grew the culture at 37°C shaker (250 rpm) until it reached an OD_{600} between 0.7-

507   0.8 (approximately 2 hours). We then diluted the culture with LB to reach an OD_{600} range

508   between 0.35-0.4. Then, we used 1 mL of the diluted outgrowth for serial dilutions until we

509   achieved 1:10,000 and 1:100,000 (outgrowth:LB) ratios. We put plates to warm up in 37°C

510   incubator for at least an hour before plating. Then, we plated both 1:10,000 and 1:100,000

511   dilutions into 2 equal sets of plates, with 12 glass beads per plate. We wrapped plates in foil to

512   avoid light exposure of aTc, and we put them in a 37°C incubator. We took the plates at 24, 28,

513   32, 44, 52, 76 and 100h post-plating to be imaged in a low-magnification microscope (see 2D

514   imaging).

515

516   **HPLC test**

517   To quantify aTc concentration from LB agar fragments, we modified the method from (Halling-

518   Sørensen et al., 2002). We used an Agilent 1220 Infinity LC instrument, and a C-18

519   chromatographic column (Aeris 3.6 μm Peptide XB-C18 100A LC column 250 x 4.6 mm). To

520   start, we directly tested aTc in the following amounts: 5 μg, 2.5 μg, 1.25 μg, 0.625 μg, 0.3125

521   μg, 0,15625 μg. From the area under peak, we generated a calibration curve and an equation

522   for aTc quantification for the following tests (Fig. S3A). We prepared triplicates of 13 mL LB agar

523   with aTc at final concentration of 100 μg/mL. Then, we poured 6 mL of each triplicate into two

524   24-well plates (1 mL/well). We prepared a total of 36 wells (triplicates for 6 reads in 2 plates). To

525   measure the aTc, we transferred the solidified media from each well to separate tubes, and we

526   diluted each with 9 mL of water. The tubes were kept in the dark and at RT for 2 hours. Then,

527   we centrifugated the tubes and filter sterilized the liquid. First, we measured triplicate samples

528   (100 μL injection each) in HPLC before any actual incubation (day 0). Then, we incubated one

529   plate for 48 hours at 37°C (the one without a set of triplicates from day 0 read), while we

530   incubated the other plate at 4°C to recreate the two possible pre-treatments, as described in

531   Colony tests section. After the first 48 hours, we also incubated the 4°C plate at 37°C, except for

532   a set of triplicates that was kept at 4°C until the end of the experiment. We continued the

533   incubation for a total of 6 days to recapitulate the actual experimental setup (see Colony tests).

534   Each day starting at day 2, we removed a set of triplicates from each plate, then, treated and

535   injected in the HPLC as explained above. Finally, we quantified aTc by measuring the area

536   under the peak for each run.

537

538   **2D imaging**

22

539 We imaged plates with colonies with a stereo microscope (Nikon SMZ800), YFP and CFP

540 fluorescence filters (Chroma #39003 and #39001, respectively), and NIS-Elements software

541 (Nikon). QS and NQS toggles are very different circuits, and therefore, have different

542 fluorescence intensities. For this reason, we used distinct settings for each circuit. We imaged

543 QS toggle colonies with an exposure time of 300 ms for YFP and CFP. While NQS toggle had

544 lower intensities, we used an exposure time of 1 s for both YFP and CFP. We manually imaged

545 each frame for CFP, YFP and bright field to form a multichannel image. Therefore, not all

546 colonies were captured from all plates. Whenever there were many colonies, we generally

547 picked 4 frames per plate to cover as many well-separated colonies as possible. We either did

548 not image or did not analyze colonies that were in contact with other colonies. We exported

549 each multichannel image into 3 separate tiff files. We assembled colony images with Fiji

550 (ImageJ). We used identical minimum and maximum fluorescence values among images in the

551 same figure to enable direct comparison, but different values across circuits. For confocal tests,

552 we also imaged colonies with the stereo microscope before any agarose was added. In such

553 images, we used the same exposure time settings for YFP and CFP for QS and NQS toggles (1

554 s for YFP and 300 ms for CFP). In Fiji, we did not use the same adjusted minimum and

555 maximum fluorescence values for QS and NQS toggles, making these images not directly

556 comparable in respect to their fluorescence intensities.

557

558 **Confocal imaging**

559 We sorted single cells into LB agar plates (see Flow cytometry), containing antibiotics and aTc

560 (25 ng/ml or 50 ng/ml). We incubated the plates at 37°C, wrapped in foil, for different times,

561 ranging from 32 to 72 hours. After growth, we covered each colony with approximately 1 mL of

562 an autoclaved 1% agarose solution. For the full colony images, we cut out pieces of agar with

563 agarose-covered colonies, we placed them upside down (with agarose on bottom) on glass

564 coverslips and took them to the Nikon A1 Confocal microscope. For the perpendicular cross-

565 section, we manually cut the pieces in the middle with a blade. We placed the middle part into a

566 glass coverslip for imaging on a Nikon A1 Confocal microscope. In the confocal, we used 405

567 nm and 488 nm lasers for excitation of CFP and YFP, respectively. We acquired images with

568 10x (for full colony Z-stacks) or 20x objective (for slices), resonant scanner, 1 A.U., with denoise

569 capture mode. For Z-stacks, steps varied from 5.1 to 15 μm distance, for a total of 200-500 μm

570 coverage within the Z axis. We exported the data into separate tiff files. We made videos with

571 Fiji (Image J). We used identical minimum and maximum fluorescence values among images

572 from the same circuit replicates to enable direct comparison, except for figures of slices. We

23

573   also captured colonies with stereo microscope (2D imaging) prior to agarose solution addition

574   for comparison.

575

576   **Data analysis**

577   We performed all data analyses in Matlab. First, we manually selected all colonies each frame,

578   and we took the average YFP and CFP fluorescence of four radii (one per direction: N, S, E, W)

579   per colony. We used the bright field for mask creation and detection of colonies. We selected

580   regions without colonies for background, which we subtracted from initial intensities. We saved

581   all data from all colonies in the same plate in a matrix per time point. We determined the yellow

582   width by measuring the distance from the center of the colony to the threshold point, in which

583   yellow fluorescence first reaches below 30% of its maximum. We then normalized this distance

584   by dividing with the total colony length (radius), giving results between 0 and 1. To obtain this

585   measure we made several assumptions: if the maximum YFP value was below a certain

586   arbitrary threshold of 200, the yellow color was considered absent, and the normalized yellow

587   width was 1 divided by total length (close to zero). If the maximum CFP value was below an

588   arbitrary threshold of 300, the blue color was considered absent, and the normalized yellow

589   width was 1. When the maximum YFP intensity at a particular pixel also had CFP above a very

590   high second threshold of 2000, this probably represented a random patch of yellow cells

591   between blue cells, and we assumed yellow was absent for purposes of width calculation.

592   Lastly, when blue was absent, and YFP showed small variation between maximum and

593   minimum (below 170), the colony was considered completely yellow, we selected the full colony

594   as the width, instead of the highest value. We picked all these arbitrary threshold values for CFP

595   and YFP through observation. We used them equally for all colonies of both circuits.

596   Furthermore, we normalized each colony's original fluorescence data by its maximum to allow

597   for color overlap analysis. We plotted each pixel from the center to the edge of the colony by its

598   normalized YFP and CFP fluorescence, and they were only classified as overlapping when both

599   YFP and CFP values were above the threshold of 0.3. Some colonies were found to have only

600   one color throughout the entire radius, for example, some of all-yellow colonies at high aTc

601   concentration. Therefore, such colonies do not show any overlap, and can skew the data. To

602   remove single color data (Fig. S4), we selected only colonies that had both colors present for at

603   least 25% of pixels. Finally, we compared all data from QS colonies to NQS. Both yellow width

604   and overlap data showed a non-normal distribution, thus, we performed non-parametric

605   statistical tests. We analyzed comparisons among 4 different aTc concentrations of the same

606   circuit with Kruskal-Wallis test (non-parametric equivalent to one-way ANOVA), followed by

24

607 multiple comparison test (Tukey-Kramer). While we analyzed direct comparison among 2 sets of

608 data with Mann-Whitney test (non-parametric equivalent to Student's t-test).

609

610 **Mathematical model**

611 **Section I – Bistability in Well-mixed Environment/Liquid Culture**

612 In the following we describe the set of equations modeling the concentrations of LacI and TetR

613 within the cells in the population. We assume that these concentrations are approximately

614 proportional to the fluorescent signals which are measured experimentally and use this

615 assumption to compare experimental and modeling results.

616 **1. Single-cell Model Derivation**

617 We let $x(t)$ and $y(t)$ represent the concentration of LacI and TetR, respectively. Assuming that

618 the intracellular concentrations of LacI and TetR are proportional the concentrations of the

619 fluorescent proteins YFP and CFP, respectively, the quantities $x(t)$ and $y(t)$ are then directly

620 related to the experimentally measured fluorescence. We therefore compare the evolution $x(t)$

621 and $y(t)$ predicted by our model to the experimentally measured fluorescence signals.

622 The production of LacI is regulated by a promoter, which can be activated by QS signaling

623 molecules (C14-HSL bound to CinR), and repressed by TetR. Similarly, production of TetR is

624 activated by the QS signal (C4-HSL bound to RhlR), and repressed by LacI. We denote by $g(t)$

625 and $h(t)$ the concentration of QS signals C14-HSL and C4-HSL at time t, respectively. We also

626 assume that LacI and TetR can be produced at maximum rates a_1 and a_2, and are degraded

627 with rate constants γ_1 and γ_2, in addition to constant dilution at rate γ_d due to cell growth. We

628 can then model the dynamics of the QS toggle using the following system of ODEs describing

629 the intracellular concentrations of LacI and TetR in one of the cells in the colony (Gardner et al.,

630 2000b; Nordholt et al., 2017; Zong et al., 2018):

$$\dot{x} = a_1\eta_1(y)\phi_1(g) - (\gamma_1 + \gamma_d)x; \tag{1a}$$

$$\dot{y} = a_2\eta_2(x)\phi_2(h) - (\gamma_2 + \gamma_d)y. \tag{1b}$$

633 The repression of the promoter is represented by Hill functions η_1 and η_2, while activation is

634 represented by Hill functions ϕ_1 and ϕ_2. In particular, we set

$$\eta_1(y(t)) = \frac{\theta_y^{n_1}}{\theta_y^{n_1} + y(t)^{n_1}}, \qquad \eta_2(x(t)) = \frac{\theta_x^{n_2}}{\theta_x^{n_2} + x(t)^{n_2}} . \tag{2a}$$

636 and

$$\phi_1(g(t)) = \frac{g(t)}{\theta_g + g(t)}, \qquad \phi_2(h(t)) = \frac{h(t)}{\theta_h + h(t)}. \tag{2b}$$

25

638 Here, the choice of Hill coefficients is based on the number of monomers in the activator (1 for
639 C14 and C4) and repressor ($n_1 = 2$ for TetR and $n_2 = 4$ for LacI).
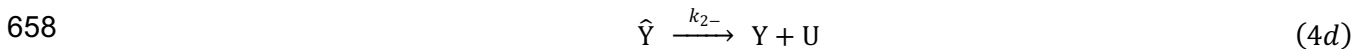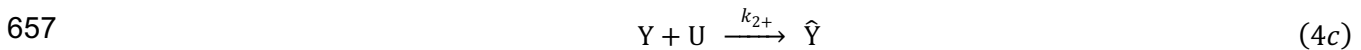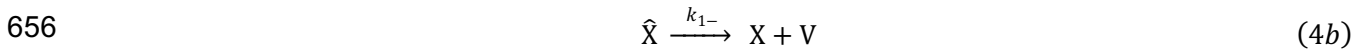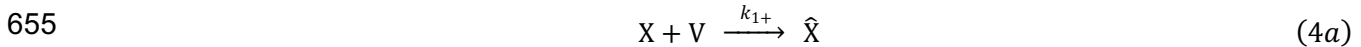
640   We model the dynamics of the intercellular QS signals, C14-HSL and C4-HSL, whose
641 activation is repressed by TetR and LacI, by the following equations,

$$\dot{g} = a_3\beta_1 + a_3(1 - \beta_1)\eta_1(y) - (\gamma_3 + \gamma_d)g; \qquad (3a)$$

$$\dot{h} = a_4\beta_2 + a_4(1 - \beta_2)\eta_2(x) - (\gamma_4 + \gamma_d)h. \qquad (3b)$$

644 Here, C14-HSL and C4-HSL are produced with maximum rate a_3 and a_4, and degraded at rate
645 γ_3 and γ_4, respectively. Further, let $a_3\beta_1$ and $a_4\beta_2$ represent the base production rate of the QS
646 signals. Setting $\phi_1(g(t)) = 1$ and $\phi_2(h(t)) = 1$ results in equations that describe the NQS
647 toggle.

648   When exogenous inducers, IPTG, and aTc, which we denote by U and V, are added to
649 the well-mixed liquid culture, the state of the system can be changed. Following experiments,
650 we will assume that IPTG and aTc are provided at some background concentration level, u_0 and
651 v_0, respectively. De-repression of the production of LacI/TetR is achieved through inducers
652 binding to their corresponding repressors. Let X and Y represent the unbound/free repressor, LacI
653 and TetR, correspondingly. If $\widehat{X}$ and $\widehat{Y}$ denote the inducer-bound complex the binding activity can
654 be described by the following reaction scheme,

$$X + V \xrightarrow{k_{1+}} \widehat{X} \qquad (4a)$$

$$\widehat{X} \xrightarrow{k_{1-}} X + V \qquad (4b)$$

$$Y + U \xrightarrow{k_{2+}} \widehat{Y} \qquad (4c)$$

$$\widehat{Y} \xrightarrow{k_{2-}} Y + U \qquad (4d)$$

659 Let $x_b(t)$ and $y_b(t)$ represent the concentration of bound LacI ($\widehat{X}$) and bound TetR ($\widehat{Y}$), we then
660 have that

$$\dot{x}_b = k_{1+}x_f v_0 - k_{1-}x_b - (\gamma_1 + \gamma_d)x_b; \qquad (5a)$$

$$\dot{y}_b = k_{2+}y_f u_0 - k_{2-}y_b - (\gamma_2 + \gamma_d)y_b. \qquad (5b)$$

663 Here, $x_f(t)$ and $y_f(t)$ represents the free LacI and TetR. By conservation law, we have that $x(t) =$
664 $x_b(t) + x_f(t)$ and $y(t) = y_b(t) + y_f(t)$.

665   Hence, the set of equations describing the dynamics of the intracellular concentrations of
666 LacI, TetR, the signaling molecules, as well as the concentrations of bound LacI and TetR is
667 given by,

$$\dot{x} = a_1\eta_1(y_f)\phi_1(g) - (\gamma_1 + \gamma_d)x; \qquad (6a)$$

$$\dot{y} = a_2\eta_2(x_f)\phi_2(h) - (\gamma_1 + \gamma_d)y; \qquad (6b)$$

26

670
$$\dot{g} = a_3\beta_1 + a_3(1 - \beta_1)\eta_1(y_f) - (\gamma_3 + \gamma_d)g; \tag{6c}$$

671
$$\dot{h} = a_4\beta_2 + a_4(1 - \beta_2)\eta_2(x_f) - (\gamma_4 + \gamma_d)h; \tag{6d}$$

672
$$\dot{x}_b = k_{1+}x_f v_0 - k_{1-} x_b - (\gamma_1 + \gamma_d)x_b; \tag{6e}$$

673
$$\dot{y}_b = k_{2+}y_f u_0 - k_{2-} y_b - (\gamma_2 + \gamma_d)y_b. \tag{6f}$$

674 **2. Nondimensionalization and Bifurcation Analysis**

675 To simplify analysis, we next assume that $\gamma_1 = \gamma_2 = \gamma$. Defining the rescaled time $\tau = (\gamma + \gamma_d)t$,

676 we can nondimensionalize each variable using its corresponding threshold to obtain the

677 following nondimensionalized QS toggle system,

678
$$\frac{d\tilde{x}}{d\tau} = \frac{\tilde{a}_1}{1 + \tilde{y}_f{}^{n_1}} \frac{\tilde{g}}{1 + \tilde{g}} - \tilde{x}; \tag{7a}$$

679
$$\frac{d\tilde{y}}{d\tau} = \frac{\tilde{a}_2}{1 + \tilde{x}_f{}^{n_2}} \frac{\tilde{h}}{1 + \tilde{h}} - \tilde{y}; \tag{7b}$$

680
$$\frac{d\tilde{g}}{d\tau} = \frac{\tilde{a}_3}{1 + \tilde{y}^{n_1}} - \tilde{\gamma}_3\tilde{g}; \tag{7c}$$

681
$$\frac{d\tilde{h}}{d\tau} = \frac{\tilde{a}_4}{1 + \tilde{x}^{n_2}} - \tilde{\gamma}_4\tilde{h}; \tag{7d}$$

682
$$\frac{d\tilde{x}_b}{d\tau} = \tilde{x}_f\tilde{v}_0 - \tilde{k}_{1-} \tilde{x}_b - \tilde{x}_b; \tag{7e}$$

683
$$\frac{d\tilde{y}_b}{d\tau} = \tilde{y}_f\tilde{u}_0 - \tilde{k}_{2-} \tilde{y}_b - \tilde{y}_b, \tag{7f}$$

684 with $\tilde{x}_f = \tilde{x} - \tilde{x}_b$ and $\tilde{y}_f = \tilde{y} - \tilde{y}_b$. Here the nondimensionalized variables and parameters are,

685
$$\tilde{x} = \frac{x}{\theta_x}; \ \tilde{y} = \frac{y}{\theta_y}; \ \tilde{g} = \frac{g}{\theta_g}; \ \tilde{h} = \frac{h}{\theta_h}; \tilde{x}_b = \frac{x_b}{\theta_x}; \ \tilde{y}_b = \frac{y_b}{\theta_y}; \ \tilde{x}_f = \frac{x_f}{\theta_x}; \ \tilde{y}_f = \frac{y_f}{\theta_y};$$

686
$$\tilde{a}_1 = \frac{a_1}{\theta_x(\gamma + \gamma_d)}; \ \tilde{a}_2 = \frac{a_2}{\theta_y(\gamma + \gamma_d)}; \ \tilde{a}_3 = \frac{a_3}{\theta_g(\gamma + \gamma_d)}; \ \tilde{a}_4 = \frac{a_4}{\theta_h(\gamma + \gamma_d)};$$

687
$$\tilde{\gamma}_3 = \frac{\gamma_3 + \gamma_d}{\gamma + \gamma_d}; \ \tilde{\gamma}_4 = \frac{\gamma_4 + \gamma_d}{\gamma + \gamma_d}; \ \tilde{v}_0 = \frac{k_{1+}v_0}{\gamma + \gamma_d}; \ \tilde{u}_0 = \frac{k_{2+}u_0}{\gamma + \gamma_d}; \ \tilde{k}_{1-} = \frac{k_{1-}}{\gamma + \gamma_d}; \ \tilde{k}_{2-} = \frac{k_{2-}}{\gamma + \gamma_d}$$

688 Eq. (7) describes the NQS toggle system after removing (7c-d) and setting $\tilde{g}/(1 + \tilde{g}) = 1$ and

689 $\tilde{h}/(1 + \tilde{h}) = 1$ in (7a-b). The nondimensionalization shows that, in the NQS toggle system, the

690 strength of the repressor, $\tilde{a}_1$ and $\tilde{a}_2$, is determined by a balance between production,

691 degradation, dilution and the repression threshold. In the QS system, the effective repressor

692 strength is modified by the QS signal profile. That is,

693
$$\tilde{a}_1^{\text{eff}}(t) = \frac{a_1}{\theta_x(\gamma + \gamma_d)}\frac{\tilde{g}(t)}{1 + \tilde{g}(t)}; \ \tilde{a}_2^{\text{eff}}(t) = \frac{a_2}{\theta_y(\gamma + \gamma_d)}\frac{\tilde{h}(t)}{1 + \tilde{h}(t)}$$

27

694   To understand how the different parameters impact the equilibria of the system, we first
695   obtain the equilibria by setting the derivatives in Eq. (7) to 0. Denoting the equilibrium values of
696   the different dynamical variables by a star, we have that, $\tilde{x}_f^*$ and $\tilde{y}_f^*$ satisfy,

697
$$F_1\left(\tilde{x}_f^*, \tilde{y}_f^*\right) := \frac{\hat{a}_1^{\text{eff}}}{1 + \tilde{y}_f^{*n_1}} - \tilde{x}_f^* = 0, \tag{8a}$$

698
$$F_2\left(\tilde{x}_f^*, \tilde{y}_f^*\right) := \frac{\hat{a}_2^{\text{eff}}}{1 + \tilde{x}_f^{*n_2}} - \tilde{y}_f^* = 0, \tag{8b}$$

699   with

700
$$\hat{a}_1^{\text{eff}} = \frac{\tilde{a}_1}{1 + \hat{v}_0} \frac{\tilde{g}^*}{1 + \tilde{g}^*}, \qquad \hat{a}_2^{\text{eff}} = \frac{\tilde{a}_2}{1 + \hat{u}_0} \frac{\tilde{h}^*}{1 + \tilde{h}^*},$$

701   and

702
$$\hat{v}_0 = \frac{\tilde{v}_0}{\tilde{k}_{1-} + 1}, \qquad \hat{u}_0 = \frac{\tilde{u}_0}{\tilde{k}_{2-} + 1}.$$

703   Let $\mathcal{L} \subset \mathbb{R}^2$ represents the bifurcation curve in the $\left(\hat{a}_1^{\text{eff}}, \hat{a}_2^{\text{eff}}\right)$ parameter space, that is the curve
704   in parameter space at which the behavior of the system changes qualitatively. Thus, crossing
705   the bifurcation curve leads to a change in the number of equilibria and/or their stability
706   (Kuznetsov, 2004). Except for the steady-state condition described in equations (8a-b), points
707   on the bifurcation curve $\mathcal{L}$ additionally must satisfy a matching slope condition (Kuznetsov,
708   2004). That is,

709
$$-\frac{\partial F_1/\partial \tilde{x}_f^*}{\partial F_1/\partial \tilde{y}_f^*}\bigg|_{\left(\hat{x}_f^*, \hat{y}_f^*\right)} = -\frac{\partial F_2/\partial \tilde{x}_f^*}{\partial F_2/\partial \tilde{y}_f^*}\bigg|_{\left(\hat{x}_f^*, \hat{y}_f^*\right)}.$$

710   After some algebra, the above condition can be simplified as following,

711
$$\hat{a}_1^{\text{eff}} \, \hat{a}_2^{\text{eff}} = n_1 n_2 \hat{x}_f^{*n_2+1} \hat{y}_f^{*n_1+1}. \tag{8c}$$

712   Solving system (8) numerically gives us the cusp bifurcation curve $\mathcal{L}$ in the $(\hat{a}_1^{\text{eff}}, \hat{a}_2^{\text{eff}})$ space, as
713   shown in Figure 2E. Nullclines plotted in Figure 2F, G are given by solving system (8a-b) for
714    $\hat{a}_1^{\text{eff}} = 3/(1 + \hat{v}_0)$ and $\hat{a}_2^{\text{eff}} = 3/(1 + \hat{u}_0)$.

715

Section II – Spatial-temporal Dynamics of the NQS and QS colony
717   Using the model of the intracellular dynamics developed above, we next describe a model of the
718   spatiotemporal dynamics of the corresponding quantities in a growing bacterial colony.
719   **1. Domain**
720   The domain, $\Omega \subseteq \mathbb{R}^3$, on which we define the model consists of two different subdomains, $\Omega =$
721    $\Omega_1 \cup \Omega_2$, with Ω_1 representing the part of the domain occupied by the bacterial colony, and Ω_2

28

722   the part occupied by the agar. The agar plate takes the shape of a cylinder, and we assume that

723   the colony takes shape of a cone (Warren et al., 2019b), as show in Fig. S7A. Assuming radial

724   symmetry, we can reduce the 3D domain to a 2D slice.

725   There are two different types of boundaries: The inner boundary, represented by $\partial\Omega^{\text{in}}$,

726   and the outer boundary, represented by $\partial\Omega$. The inner boundary is the interface between the

727   colony subdomain, Ω_1, and the agar subdomain, Ω_2. The outer boundary is the union of the

728   colony-air interface and the agar-plate interface.

729   The colony is observed experimentally over tens of hours during which it can grow

730   substantially. We therefore include colony growth in the model. Previously, Warren et al. (2019)

731   have identified three phases of colony expansion: The initial monolayer phase (0-13 h); the

732   establishment phase (14-24 h); the flattening phase (24+ h). In the establishment phase, growth

733   in both height and radius is linear, as cells predominantly divide in the active growing region

734   consisting of a thin disk at the bottom of the colony of approximate height $H_{\text{AGL}} = 10\ \mu m$. During

735   the flattening phase, radial growth is still linear while the increase in height slows.

736   In our case, the observed pattern in both the NQS and QS colony is driven by diffusive

737   signals. Since the size the colony is much smaller than the characteristic length scale of signal

738   diffusion during the experiments, details quantitative description on how the colony grows

739   vertically do not matter much. Therefore, for simplicity we assume that the colony expands

740   linearly in both radius and height, with a thin actively growing layer on the bottom. These

741   assumptions together imply a fixed aspect ratio in colony height vs radius. In our simulation, the

742   continuous growth of the colony is discretized by adding slabs of uniform heights and linearly

743   increasing radius every unit time. In particular, in experiment the radius of the colony by the end

744   of 100 hours is approximately $4\ mm$, giving a linear radius growth rate of $v_r = 40\ \mu m/h$.

745   Moreover, the cross-sectional images of the colony show that at different times of colony

746   expansion, the height to radius ratio ranges from $1:7$ to $1:12$. For simplicity, we assume a fixed

747   ratio of the height to base in the triangular slice to be $1:10$, which leads to a linear height growth

748   rate of $v_h = 4\ \mu m/h$.
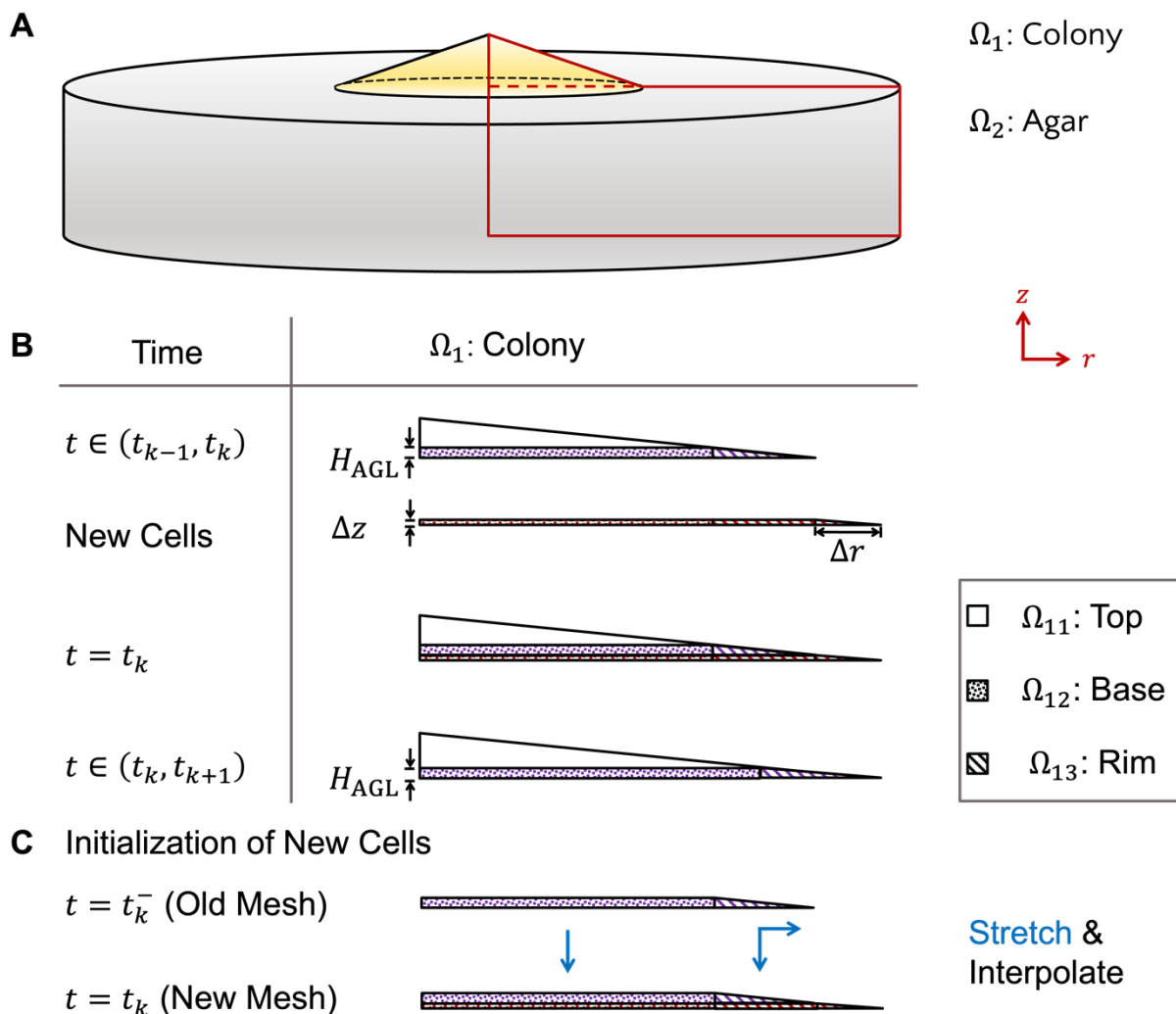
29

Supplement Figure 7: Schematics of the 3D domain and the discretization of the colony expansion used in numerical simulations. A) We assume a cone shaped growing colony sits on top of the cylindrical agar pad. The red curves outline a 2D slice from the 3D domain, in the radial (r) and height (z) direction. Assuming radial symmetry, which is consistent with experimental observations, we used this 2D slice as the domain for the model. The solid line represents the outer boundary ($\partial\Omega$) while the dashed line represents the inner boundary ($\partial\Omega^{\mathrm{in}}$). **B)** Growth is modeled by updating the colony's shape at even increments in time, Δt. At the end of each subinterval, the domain of the colony, Ω_1, is increased by adding a rectangle of height Δz and of width equal to that of the colony, and an adjoining right triangle of height Δz with base Δr. Here, we discretize time into intervals (t_{k-1}, t_k), with $t_k = k \cdot \Delta t$. **C)** After every increment of time, a new mesh is generated for the expanded colony. The new nodes at the Top and Rim region are initialized by interpolating the solution of the corresponding region from the stretched old mesh.

As shown in Fig. S7B, based on growth assumption at different locations, we divide the colony subdomain Ω_1 into three different regions, top (Ω_{11}), base (Ω_{12}), and rim (Ω_{13}). In particular, the triangular top, defined as $\Omega_{11} = \{(r, z) \in \Omega_1 | z \geq H_{\mathrm{AGL}}\}$, doesn't grow. Let R_k

30

765   represents the radial length of the colony at the end of time intervals (t_{k-1}, t_k). The rectangular

766   base, defined as $\Omega_{12} = \{(r, z) \in \Omega_1 | r \leq R_k, z \leq H_{AGL}\}$, grows linearly only in the vertical

767   direction. The triangular rim, defined as $\Omega_{13} = \{(r, z) \in \Omega_1 | r \geq R_k\}$, grows linearly in both the

768   vertical and radial direction.

769   Let T be the time it takes for the colony to grow H_{AGL} in the vertical direction. Here, $T =$

770    $H_{AGL}/v_h = 150\ min$. Let S_k^{12} represents the area of the top region, Ω_{12}, at the end of time interval

771   (t_{k-1}, t_k), where $S_k^{12} = H_{AGL}R_k$. Then we have that

772
$$\frac{S_{k+1}^{12} - S_k^{12}}{\Delta t} = \frac{\Delta H}{\Delta t}R_k = \frac{H_{AGL}}{T}R_k = \frac{1}{T}S_k^{12}.$$

773   Similarly, let S_k^{13} represents the area of the rim region, Ω_{13}, at the end of time interval (t_{k-1}, t_k),

774   where $S_k^{13} = \kappa H_{AGL}^2/2$, with κ represent the fixed radius-height ratio of the colony. Then we have

775
$$\frac{S_{k+1}^{13} - S_k^{13}}{\Delta t} = \frac{\Delta H}{\Delta t}\kappa\left(H_{AGL} + \frac{1}{2}\Delta H\right) = \frac{H_{AGL}}{T}\kappa\left(H_{AGL} + \frac{1}{2}\Delta H\right) = \frac{2}{T}S_k^{13} + O(\Delta H).$$

776   Therefore, we can approximate the expansion factor of the rim region, Ω_{13}, by $2/T$, which is

777   twice as fast as the expansion rate base region, Ω_{12}. Let $\gamma_d = 1/T$, we then get that the

778   following chemical dilution rate from colony expansion in the different regions,

779
$$\gamma_d(X) = \begin{cases} 0, & X \in \Omega_{11}; \\ \gamma_d, & X \in \Omega_{12}; \\ 2\gamma_d, & X \in \Omega_{13}. \end{cases}$$

780

781   **2. PDE Model**

782   Let $u(X, t)$ represent the aTc concentration at time t and location $X \in \Omega$. The inducer, aTc, is

783   initially supplied in the agar, which then diffuses into the colony and react with TetR in different

784   cells. The reaction occurring within the cells in the colony can be modeled using Eqs. $(4c, d)$.

785   We assume that when the aTc-TetR complex, $\hat{Y}$, is being degraded by the enzyme ClpXP, and

786   that a portion $\alpha \in [0,1]$ of the aTc returns to the cell from the complex (Nevozhay et al., 2009).

787   That is,

789
$$\hat{Y} \xrightarrow{\alpha(\gamma_2 + \gamma_d(X))} \emptyset + U.$$

788

790   Putting everything together, for the concentrations of,

791   x: [LacI]; y_f: [free TetR]; y_b: [bound TetR]; g: [C14]; h: [C4]; u: [aTc],

792   with $y = y_f + y_b$, and the superscript represent different subdomain, we obtain a diffusion-

793   reaction model we describe next.

794   In the colony domain, $X \in \Omega_1$, the various concentrations evolve according to,

31

$$\frac{\partial x}{\partial t} = a_1 \eta_1(y_f)\phi_1(g) - (\gamma_1 + \gamma(X))x, \tag{9a}$$

$$\frac{\partial y}{\partial t} = a_2 \eta_2(x)\phi_2(h) - (\gamma_2 + \gamma(X))y, \tag{9b}$$

$$\frac{\partial y_b}{\partial t} = k_{2+}u^c y_f - k_{2-}\,y_b - (\gamma_2 + \gamma(X))y_b, \tag{9c}$$

$$\frac{\partial g^c}{\partial t} = D_1^c \Delta g^c + a_3\beta_1 + a_3(1-\beta_3)\eta_1(y_f) - (\gamma_3 + \gamma(X))g^c, \tag{9d}$$

$$\frac{\partial h^c}{\partial t} = D_2^c \Delta h^c + a_4\beta_4 + a_4(1-\beta_4)\eta_2(x) - (\gamma_4 + \gamma(X))h^c, \tag{9e}$$

$$\frac{\partial u^c}{\partial t} = D_3^c \Delta u^c - k_{2+}u^c y_f + k_{2-}y_b + \alpha(\gamma_2 + \gamma_d(X))\,y_b - (\gamma_5 + \gamma(X))u^c. \tag{9f}$$

In the agar domain, Ω_2, we have

$$\frac{\partial g^a}{\partial t} = D_1^a \Delta g^a - \gamma_3 g^a, \tag{9g}$$

$$\frac{\partial h^a}{\partial t} = D_2^a \Delta h^a - \gamma_4 h^a, \tag{9h}$$

$$\frac{\partial u^a}{\partial t} = D_3^a \Delta u^a - \gamma_5 u^a. \tag{9i}$$

Here D_i^a denotes the signal diffusion coefficient in agar, for different chemicals C14, C4 and aTc indexed by $i = 1,2,3$ respectively. Due to the crowdedness of the colony, we assume that signal diffusion coefficients in the colony, D_i^c, satisfies $D_i^c < D_i^a$. In particular, it has been shown that GFP diffuse 10 times faster in water ($D_{\mathrm{GFP}}^{\mathrm{aqua}} \approx 87\mu m^2/s$)(Swaminathan et al., 1997), compared with in the cytoplasm ($D_{\mathrm{GFP}}^{\mathrm{cyto}} \approx 8\mu m^2/s$) (Elf et al., 2007). Therefore, we set $D_i^a = 10D_i^c$. Since aTc has a lower molecular weight than GFP, we assume that the aTc diffusion coefficient in agar is $D_1^a = 400\ \mu m^2/s$. It has been reported that the effective diffusion coefficients of C14 and C4 are $D_{\mathrm{C14}} \approx 83\mu m^2/s$ and $D_{\mathrm{C4}} \approx 1810\mu m^2/s$ (Karig et al., 2018). Here we set the diffusion coefficients in agar to $D_2^a = 10^2\ \mu m^2/s$ and $D_3^a = 10^3\ \mu m^2/s$, for C14 and C4, respectively.

For the diffusible chemicals, $C = g, h,$ or u, we also we the following inner and outer boundary conditions.

$$C^a(X,t)|_{X \in \partial\Omega^{\mathrm{in}}} = C^c(X,t)|_{X \in \partial\Omega^{\mathrm{in}}}, \tag{9j}$$

$$\boldsymbol{n} \cdot D_i^a \nabla C^a(X,t)|_{X \in \partial\Omega^{\mathrm{in}}} = -\boldsymbol{n} \cdot D_i^c \nabla C^c(X,t)|_{X \in \partial\Omega^{\mathrm{in}}}, \tag{9k}$$

$$\boldsymbol{n} \cdot D_i^{a/c} \nabla C^{a/c}(X,t)\big|_{X \in \partial\Omega} = 0. \tag{9l}$$

We used the radial symmetry of the 3D domain to reduce it to an equivalent 2D model. Let r and z represent the independent variables denotes the radius and height coordinate inside the colony. We then have that the Laplacian operator acts on $C = g, h,$ or u as

32

822
$$\Delta C = \frac{1}{r}\frac{\partial}{\partial r}\left(r\frac{\partial C}{\partial r}\right) + \frac{\partial C}{\partial z}.$$

823

Parameters and Simulation

824

825   We assume the tagged degradation gives a half-life of $7 \ \text{min}$ for intercellular species (Chen et

826   al., 2015). This leads to degradation rates of LacI and TetR of $\gamma = \gamma_1 = \gamma_2 = \ln(2)/7 \ \text{min}^{-1}$. It

827   has been reported that the degradation rate of AHL ranges from zero (no detectable

828   degradation at 32 hours) to a half-life of 8 hours depending on environmental factors such as

829   temperature and pH value (Politi et al., 2014). For our experimental condition, we assume that

830   the half-life of C14 and C4 is 24 hours, corresponding to degradation rates of $\gamma_3 = \gamma_4 =$

831    $\ln(2)/24 \ h^{-1}$. The production rates of each species, a_i, with $i = 1,\ldots,4$ along with their

832   corresponding threshold of activation (EC50)/repression (IC50) parameters θ_j, with $j =$

833    $\{x, y, g, h\}$, were chosen so that the nondimensionalized parameters, $\tilde{a}_i$, give a match with

834   experimentally observed patterns. We also set the basal production level of the AHL signals to

835    $\beta_1 = 0.2$ and $\beta_1 = 0.5$, for C14 and C4 respectively. It has been reported that aTc bind with TetR

836   at rate, $k_+ = 0.06/\text{nM/min}$ (Nevozhay et al., 2009). As shown in Fig 1E and G, aTc can induce

837   the yellow state at a concentration of 1 ng/ml in the NQS, and at approximately 10 ng/ml in the

838   QS case. Therefore, we set $k_+ = k \cdot 0.06 \ \text{nM}^{-1}\text{min}^{-1}$, with $k = 1$ in the NQS case and $k = 10$ in

839   the QS case. We set the unbinding rate to $k_- = k_+/k_A$, with association constant $k_A = 10 \ \text{nM}^{-1}$

840   (Kintrup et al., 2000). When the aTc-TetR complex is degraded by ClpXP, we assume that $\alpha =$

841   0.8 portion of the aTc in the complex returns back to the cell. All parameters used in Figure

842   7C,D are the same as those used in Figure 7B except the following: in Figure 7C, a pulse of $\gamma =$

843    $\ln(2)/5.178 \ \text{min}^{-1}$ between $t = 23.25 \ \text{hr}$ and $t = 25.575 \ \text{hr}$ is applied; in Figure 7D, repressor

844   strengths are reduced to $a_1 = 80 \ \text{nM/min}$ and $a_2 = 120 \ \text{nM/min}$.

845   We simulate the PDE-ODE model, described by Eqs. (9) using MATLAB. To reduce

846   interpolation error, we took the following approach: First, over $\delta t = 1\text{min}$ time intervals, the

847   PDEs were solved using the Partial Differential Equation Toolbox and the ODEs were solved

848   using ode15s at each mesh point, using the solution from the previous time step as initial

849   conditions. Second, the mesh for subdomain Ω_{11}, the top of the colony, was kept the same

850   between each update of the colony size at every $\Delta t = 15 \ \text{min}$. Meanwhile, at each colony

851   growth update time point $t = t_k$, as shown in Figure S1B, mesh points in the bottom layer (Ω_{12}

852   and Ω_{13}) were initialized by interpolating the solution at $t = t_k^-$ with the coordinates of the mesh

853   points linearly stretched, as shown in Figure S1C.

854

33

855 **Supplemental information titles and legends**

856 **Supplemental Figure 1: Individual behavior of QS and NQS toggle cells when treated with**

857 **a single inducer for different duration of times.** Flow cytometry data of QS and NQS toggle

858 cells that were pre-induced with either IPTG or aTc. Each dot is a single cell classified within a

859 gate. Gates were determined with single color and double negative controls. Dashed lines in each

860 plot represent the boundaries between the three distinct gates, which represent cellular states:

861 CFP+ (top gate), YFP+ (bottom-right gate), and OFF (bottom-left gate). Background colors in

862 each plot represent which state the majority of cells are in (>50%): blue color indicates mostly

863 CFP+ cells, yellow plots are mostly YFP+, gray plots are mostly OFF, and white plots indicate

864 cells that are present in multiple states (<50% each). **A)** QS toggle cells pre-treated with IPTG

865 and aTc after growth for 3 (top), 9 (middle), and 12 hours (bottom). **B)** NQS toggle cells pre-

866 treated with IPTG and aTc after growth for 3 (top) and 9 hours (bottom) (see Fig. 2).

867

868 **Supplemental Figure 2: Induction curves of circuit variations of the QS toggle.** We obtained

869 the Weaker Blue State by using lower strength promoters for *tetR* and *cfp* genes. We obtained

870 the Weaker QS toggle by using lower strength promoters for the circuit genes, except both QS

871 genes which were kept the same. We obtained the Inverted QS toggle by using the same lower

872 strength promoters but reversing the QS network connected to each state: now, the rhlR/I network

873 activates the yellow state, and cinR/I the blue state. **A, B)** Induction curves of Weaker Blue State

874 QS toggle with IPTG (A) and aTc (B) in liquid culture. **C, D)** Induction curves of Weaker QS toggle

875 with IPTG (C) and aTc (D) in liquid culture. **E, F)** Induction curves of Weaker QS toggle with IPTG

876 (E) and aTc (F) in liquid culture, in which cells were pre-treated with IPTG. **G, H)** Induction curves

877 of weaker QS toggle with IPTG (G) and aTc (H) in liquid culture, in which cells were pre-treated

878 with aTc. **I, J)** Induction curves of Inverted QS toggle with IPTG (I) and aTc (J) in liquid culture.

879 Lines represent the average fluorescence and error bars represent the standard deviation of 3

880 technical replicates for at least 3 independent experiments (see Fig. 1).

881

882 **Supplemental Figure 3: Incubation at 37°C causes aTc degradation. A)** Yellow ring width

883 measured from QS toggle colonies grown in aTc plates pre-incubated either at 4°C or 37°C for

884 48 hours prior to plating. Then, we plated and grew cells as shown in Fig. 3A. These values

885 represent yellow ring widths from 76h post-plating. The 37°C plates showed a significant decrease

886 in width in comparison to its 4°C counterparts, except at 12.5 ng/ml (*p < 0.01, Mann-Whitney

887 non-parametric test). Data is from 5 independent experiments. Pre-4°C colonies are included in

888 Fig. 3B. **B)** ATc quantification from LB agar extracts (in the absence of cells) with an HPLC. At

34

889   time 0, aTc was quantified before any incubation. Samples were divided in two groups: pre-

890   incubation for 48 hours at 37°C (bright blue), or 4°C (light blue) to recreate the experimental

891   timeline in (A). On day 2, we incubated both groups at 37°C until day 6 to also recapitulate the

892   experimental setup. As a control (gray), LB agar + aTc samples were kept at 4°C throughout the

893   entire test and measured on day 7. Data represents mean ± standard deviation of 3 independent

894   experiments (see Fig. 3).

895

896   **Supplemental Figure 4: Quantification of pixel overlap for QS toggle (light gray) and NQS**

897   **toggle (dark gray) colonies without single color data.** We selected only colonies that have

898   both colors present for at least 25% of the radius. We normalized the number of overlapping pixels

899   by the colony radius (total pixels) ($p < 0.01$, Mann-Whitney non-parametric test). Data for each

900   QS toggle test contains over 138 colonies from at least 11 independent experiments, while data

901   for each NQS test contains at least 5 colonies from 2 independent experiments (see Fig. 4).

902

903   **Supplemental Figure 5: Multiple blue rings are also observed in LB agar QS colonies. A)**

904   Example of colony obtained from a 50 ng/ml aTc plate, over time. **B, C)** Fluorescence intensity

905   cross-section at 52h and 76h, respectively, shown in (A). Curves are the average fluorescence

906   between 4 radii of the same colony. **D, E)** We plotted each colony pixel from the images at 52h

907   and 76h, respectively, for both normalized fluorescence values. We classified pixels as

908   overlapping when both normalized fluorescence values were above a threshold of 0.3 (inside the

909   gray boxed region). Curves are the average fluorescence between 4 radii of the same colony. **F)**

910   Example of imperfectly symmetrical internal blue rings from a different colony at 52 hours post-

911   plating (see Fig. 7).

912

913   **Supplemental Figure 6: Expanding QS colonies in EZ rich defined medium. A)** Colonies

914   obtained from plates with different aTc concentrations, over time. At 100 ng/ml aTc, colonies

915   remained all yellow or with blue center or internal ring fragments. **B)** We used the measurement

916   of color overlap to quantify the spatial segregation of states per colony. We classified pixels as

917   overlapping when both normalized fluorescence values were above a threshold of 0.3.

918   Measurement of overlap was normalized by the colony radius (total number of pixels). Data is

919   from 2 independent experiments. **C)** Fluorescence intensity cross-sectionals of colonies shown in

920   (A). Curves are the average fluorescence between 4 radii of the same colony (see Fig. 7).

921

35

922   **Supplement Figure 7: Schematics of the 3D domain and the discretization of the colony**

923   **expansion used in numerical simulations. A)** We assume a cone shaped growing colony sits

924   on top of the cylindrical agar pad. The red curves outline a 2D slice from the 3D domain, in the

925   radial (r) and height (z) direction. Assuming radial symmetry, which is consistent with

926   experimental observations, we used this 2D slice as the domain for the model. The solid line

927   represents the outer boundary ($\partial\Omega$) while the dashed line represents the inner boundary ($\partial\Omega^{\mathrm{in}}$).

928   **B)** Growth is modeled by updating the colony's shape at even increments in time, Δt. At the end

929   of each subinterval, the domain of the colony, Ω_1, is increased by adding a rectangle of height

930   Δz and of width equal to that of the colony, and an adjoining right triangle of height Δz with base

931   Δr. Here, we discretize time into intervals (t_{k-1}, t_k), with $t_k = k \cdot \Delta t$. **C)** After every increment of

932   time, a new mesh is generated for the expanded colony. The new nodes at the Top and Rim

933   region are initialized by interpolating the solution of the corresponding region from the stretched

934   old mesh (see Fig. 5).

935

936   **Supplement Movie 1: Patterning in the expanding NQS toggle colony.** Once aTc drops

937   below the hysteresis point, cells from the top start to switch to the blue state. Sequestration and

938   degradation of aTc leads to the further spreading of the blue wave. Top: aTc profile at different

939   locations of the colony. Middle: 2D colormap of the LacI and TetR profile at different locations of

940   the colony. Bottom three panels on left: normalized LacI and TetR concentration in the top-down

941   view of the colony. Bottom right: Evolution of the effective promoter strength at the top and rim

942   of the colony.

943

944   **Supplement Movie 2: Patterning in the expanding QS toggle colony.** Faster growth and

945   balance of the QS signals at the rim leads to cells switching to the blue state. Bistability in the

946   non-growing top leads to preservation of the yellow/blue states, as new cells are pushed out of

947   the actively growing layer. This leads to a stable switching boundary in the radial direction. Top:

948   aTc profile at different locations of the colony. Middle: 2D colormap of the LacI and TetR profile

949   at different locations of the colony. Bottom three panels on left: normalized LacI and TetR

950   concentration in the top-down view of the colony. Bottom right: Evolution of the effective

951   promoter strength at the top and rim of the colony.

952

953

954

955

References

956
957 Alaynick, W. A., Jessell, T. M., & Pfaff, S. L. (2011). SnapShot: Spinal cord development. *Cell*,
958   *146*(1), 178.e1-178.e1. https://doi.org/10.1016/j.cell.2011.06.038
959 Barbier, I., Perez-Carrasco, R., & Schaerli, Y. (2020). Controlling spatiotemporal pattern
960   formation in a concentration gradient with a synthetic toggle switch. *Molecular Systems*
961   *Biology*, *16*(6), 1–15. https://doi.org/10.15252/msb.20199361
962 Benner, S. A., & Sismour, A. M. (2005). Synthetic biology. *Nature Reviews Genetics*, *6*(7), 533–
963   543. https://doi.org/10.1038/nrg1637
964 Briscoe, J., & Small, S. (2015). Morphogen rules: Design principles of gradient-mediated
965   embryo patterning. *Development (Cambridge)*, *142*(23), 3996–4009.
966   https://doi.org/10.1242/dev.129452
967 Cachat, E., Liu, W., & Davies, J. A. (2017). Synthetic self-patterning and morphogenesis in
968   mammalian cells: a proof-of-concept step towards synthetic tissue development.
969   *Engineering Biology*, *1*(2), 71–76. https://doi.org/10.1049/enb.2017.0013
970 Callura, J. M., Cantor, C. R., & Collins, J. J. (2012). Genetic switchboard for synthetic biology
971   applications. *Proceedings of the National Academy of Sciences of the United States of*
972   *America*, *109*(15), 5850–5855. https://doi.org/10.1073/pnas.1203808109
973 Cameron, D. E., Bashor, C. J., & Collins, J. J. (2014). A brief history of synthetic biology. *Nature*
974   *Reviews Microbiology*, *12*(5), 381–390. https://doi.org/10.1038/nrmicro3239
975 Cao, Y., Ryser, M. D., Payne, S., Li, B., Rao, C. V., & You, L. (2016a). Collective Space-
976   Sensing Coordinates Pattern Scaling in Engineered Bacteria. *Cell*, *165*(3), 620–630.
977   https://doi.org/10.1016/j.cell.2016.03.006
978 Cao, Y., Ryser, M. D., Payne, S., Li, B., Rao, C. v., & You, L. (2016b). Collective Space-Sensing
979   Coordinates Pattern Scaling in Engineered Bacteria. *Cell*, *165*(3), 620–630.
980   https://doi.org/10.1016/j.cell.2016.03.006
981 Chen, Y., Kim, J. K., Hirning, A. J., Josić, K., & Bennett, M. R. (2015). Emergent genetic
982   oscillations in a synthetic microbial consortium. *Science*, *349*(6251), 986–989.
983   https://doi.org/10.1126/science.aaa3794
984 Cheng, A. A., & Lu, T. K. (2012). Synthetic Biology An emerging engineering discipline. *Annual*
985   *Review of Biomedical Engineering*, *14*(April), 155–178. https://doi.org/10.1146/annurev-
986   bioeng-071811
987 Church, G. M., Elowitz, M. B., Smolke, C. D., Voigt, C. A., & Weiss, R. (2014). Realizing the
988   potential of synthetic biology. *Nature Reviews Molecular Cell Biology*, *15*(4), 289–294.
989   https://doi.org/10.1038/nrm3767
990 Curatolo, A. I., Zhou, N., Zhao, Y., Liu, C., Daerr, A., Tailleur, J., & Huang, J. (2020).
991   Cooperative pattern formation in multi-component bacterial systems through reciprocal
992   motility regulation. *Nature Physics*, *16*(11), 1152–1157. https://doi.org/10.1038/s41567-
993   020-0964-z
994 Davies, J. A., & Glykofrydis, F. (2020). Engineering pattern formation and morphogenesis.
995   *Biochemical Society Transactions*, *48*(3), 1177–1185.
996   https://doi.org/10.1042/BST20200013
997 Dessaud, E., McMahon, A. P., & Briscoe, J. (2008). Pattern formation in the vertebrate neural
998   tube: A sonic hedgehog morphogen-regulated transcriptional network. *Development*,
999   *135*(15), 2489–2503. https://doi.org/10.1242/dev.009324

37

1000 Diambra, L., Senthivel, V. R., Menendez, D. B., & Isalan, M. (2015). Cooperativity to increase
1001   turing pattern space for synthetic biology. *ACS Synthetic Biology*, *4*(2), 177–186.
1002   https://doi.org/10.1021/sb500233u
1003 Elf, J., Li, G.-W., & Xie, X. S. (2007). Probing Transcription Factor Dynamics at the Single-
1004   Molecule Level in a Living Cell. *Science*, *316*(5828), 1191–1194.
1005   https://doi.org/10.1126/science.1141967
1006 Gardner, T. S., Cantor, C. R., & Collins, J. J. (2000a). Construction of a genetic toggle switch in
1007   Escherichia coli. *Nature*, *403*(6767), 339–342. https://doi.org/10.1038/35002131
1008 Gardner, T. S., Cantor, C. R., & Collins, J. J. (2000b). Construction of a genetic toggle switch in
1009   Escherichia coli. In *NATURE* (Vol. 403). www.nature.com
1010 Grant, P. K., Szep, G., Patange, O., Halatek, J., Coppard, V., Csikász-Nagy, A., Haseloff, J.,
1011   Locke, J. C. W., Dalchau, N., & Phillips, A. (2020). Interpretation of morphogen gradients
1012   by a synthetic bistable circuit. *Nature Communications*, *11*(1), 1–8.
1013   https://doi.org/10.1038/s41467-020-19098-w
1014 Halling-Sørensen, B., Sengeløv, G., & Tjørnelund, J. (2002). Toxicity of tetracyclines and
1015   tetracycline degradation products to environmentally relevant bacteria, including selected
1016   tetracycline-resistant bacteria. *Archives of Environmental Contamination and Toxicology*,
1017   *42*(3), 263–271. https://doi.org/10.1007/s00244-001-0017-2
1018 Karig, D., Michael Martini, K., Lu, T., DeLateur, N. A., Goldenfeld, N., & Weiss, R. (2018a).
1019   Stochastic Turing patterns in a synthetic bacterial population. *Proceedings of the National
1020   Academy of Sciences of the United States of America*, *115*(26), 6572–6577.
1021   https://doi.org/10.1073/pnas.1720770115
1022 Karig, D., Michael Martini, K., Lu, T., DeLateur, N. A., Goldenfeld, N., & Weiss, R. (2018b).
1023   Stochastic Turing patterns in a synthetic bacterial population. *Proceedings of the National
1024   Academy of Sciences of the United States of America*, *115*(26), 6572–6577.
1025   https://doi.org/10.1073/pnas.1720770115
1026 Khalil, A. S., & Collins, J. J. (2010). Synthetic biology: Applications come of age. *Nature
1027   Reviews Genetics*, *11*(5), 367–379. https://doi.org/10.1038/nrg2775
1028 Kim, H., Jin, X., Glass, D. S., & Riedel-Kruse, I. H. (2020). Engineering and modeling of
1029   multicellular morphologies and patterns. *Current Opinion in Genetics and Development*,
1030   *63*(Figure 1), 95–102. https://doi.org/10.1016/j.gde.2020.05.039
1031 Kintrup, M., Schubert, P., Kunz, M., Chabbert, M., Alberti, P., Bombarda, E., Schneider, S., &
1032   Hillen, W. (2000). Trp scanning analysis of Tet repressor reveals conformational changes
1033   associated with operator and anhydrotetracycline binding. *European Journal of
1034   Biochemistry*, *267*(3), 821–829. https://doi.org/10.1046/j.1432-1327.2000.01063.x
1035 Kuznetsov, Y. A. (2004). *Elements of Applied Bifurcation Theory* (Vol. 112). Springer New York.
1036   https://doi.org/10.1007/978-1-4757-3978-7
1037 Lithgow, J. K., Wilkinson, A., Hardman, A., Rodelas, B., Wisniewski-Dyé, F., Williams, P., &
1038   Downie, J. A. (2000). The regulatory locus cinRI in Rhizobium leguminosarum controls a
1039   network of quorum-sensing loci. *Molecular Microbiology*, *37*(1), 81–97.
1040   https://doi.org/10.1046/j.1365-2958.2000.01960.x
1041 Liu, C., Fu, X., Liu, L., Ren, X., Chau, C. K. L., Li, S., Xiang, L., Zeng, H., Chen, G., Tang, L.-H.,
1042   Lenz, P., Cui, X., Huang, W., Hwa, T., & Huang, J.-D. (2011). Sequential Establishment of

Stripe Patterns in an Expanding Cell Population Chenli. *Science*, *334*(October), 238–242. https://doi.org/10.7551/mitpress/8876.003.0036

Lugagne, J. B., Sosa Carrillo, S., Kirch, M., Köhler, A., Batt, G., & Hersen, P. (2017). Balancing a genetic toggle switch by real-time feedback control and periodic forcing. *Nature Communications*, *8*(1), 1–7. https://doi.org/10.1038/s41467-017-01498-0

McCarty, N. S., & Ledesma-Amaro, R. (2019). Synthetic Biology Tools to Engineer Microbial Communities for Biotechnology. *Trends in Biotechnology*, *37*(2), 181–197. https://doi.org/10.1016/j.tibtech.2018.11.002

Nasiadka, A., Dietrich, B. H., & Krause, H. M. (2002). Anterior-posterior patterning in the Drosophila embryo. *Advances in Developmental Biology and Biochemistry*, *12*(C), 155–204. https://doi.org/10.1016/S1569-1799(02)12027-2

Nevozhay, D., Adams, R. M., Murphy, K. F., Josić, K., & Balázsi, G. (2009). Negative autoregulation linearizes the dose–response and suppresses the heterogeneity of gene expression. *Proceedings of the National Academy of Sciences*, *106*(13), 5123–5128. https://doi.org/10.1073/pnas.0809901106

Nikolaev, E. V., & Sontag, E. D. (2016). Quorum-Sensing Synchronization of Synthetic Toggle Switches: A Design Based on Monotone Dynamical Systems Theory. *PLoS Computational Biology*, *12*(4). https://doi.org/10.1371/journal.pcbi.1004881

Nordholt, N., van Heerden, J., Kort, R., & Bruggeman, F. J. (2017). Effects of growth rate and promoter activity on single-cell protein expression. *Scientific Reports*, *7*(1). https://doi.org/10.1038/s41598-017-05871-3

Payne, S., Li, B., Cao, Y., Schaeffer, D., Ryser, M. D., & You, L. (2013). Temporal control of self-organized pattern formation without morphogen gradients in bacteria. *Molecular Systems Biology*, *9*(1), 1–10. https://doi.org/10.1038/msb.2013.55

Pesci, E. C., Pearson, J. P., Seed, P. C., & Iglewski, B. H. (1997). Regulation of las and rhl quorum sensing in Pseudomonas aeruginosa. *Journal of Bacteriology*, *179*(10), 3127–3132. https://doi.org/10.1128/jb.179.10.3127-3132.1997

Politi, N., Pasotti, L., Zucca, S., Casanova, M., Micoli, G., Cusella De Angelis, M. G., & Magni, P. (2014). Half-life measurements of chemical inducers for recombinant gene expression. *Journal of Biological Engineering*, *8*(1). https://doi.org/10.1186/1754-1611-8-5

Potvin-Trottier, L., Lord, N. D., Vinnicombe, G., & Paulsson, J. (2016). Synchronous long-term oscillations in a synthetic gene circuit. *Nature*, *538*(7626), 514–517. https://doi.org/10.1038/nature19841

Riglar, D. T., Richmond, D. L., Potvin-Trottier, L., Verdegaal, A. A., Naydich, A. D., Bakshi, S., Leoncini, E., Lyon, L. G., Paulsson, J., & Silver, P. A. (2019). Bacterial variability in the mammalian gut captured by a single-cell synthetic oscillator. *Nature Communications*, *10*(1). https://doi.org/10.1038/s41467-019-12638-z

Santos-Moreno, J., & Schaerli, Y. (2018). Using Synthetic Biology to Engineer Spatial Patterns. *Advanced Biosystems*, *3*(4), 1–15. https://doi.org/10.1002/adbi.201800280

Sekine, R., Shibata, T., & Ebisuya, M. (2018). Synthetic mammalian pattern formation driven by differential diffusivity of Nodal and Lefty. *Nature Communications*, *9*(1), 1–11. https://doi.org/10.1038/s41467-018-07847-x

Struhl, G. (1989). Differing strategies for organizing anterior and posterior body pattern in Drosophila embryos. *Nature*, *338*(6218), 741–744. https://doi.org/10.1038/338741a0

39

1087 Swaminathan, R., Hoang, C. P., & Verkman, A. S. (1997). Photobleaching recovery and
1088   anisotropy decay of green fluorescent protein GFP-S65T in solution and cells: Cytoplasmic
1089   viscosity probed by green fluorescent protein translational and rotational diffusion.
1090   *Biophysical Journal*, *72*(4), 1900–1907. https://doi.org/10.1016/S0006-3495(97)78835-0
1091 Turing, A. M. (1952). The chemical basis of morphogenesis. *Philosophical Transactions of the*
1092   *Royal Society B: Biological Sciences*, *237*(August), 37–72.
1093 Wang, L., Walker, B. L., Iannaccone, S., Bhatt, D., Kennedy, P. J., & Tse, W. T. (2009). Bistable
1094   switches control memory and plasticity in cellular differentiation. *Proceedings of the*
1095   *National Academy of Sciences of the United States of America*, *106*(16), 6638–6643.
1096   https://doi.org/10.1073/pnas.0806137106
1097 Warren, M. R., Sun, H., Yan, Y., Cremer, J., Li, B., & Hwa, T. (2019a). Spatiotemporal
1098   establishment of dense bacterial colonies growing on hard agar. *ELife*, *8*, 1–47.
1099   https://doi.org/10.7554/eLife.41093
1100 Warren, M. R., Sun, H., Yan, Y., Cremer, J., Li, B., & Hwa, T. (2019b). *Spatiotemporal*
1101   *establishment of dense bacterial colonies growing on hard agar*.
1102   https://doi.org/10.7554/eLife.41093.001
1103 Weisenberger, M. S., & Deans, T. L. (2018). Bottom-up approaches in synthetic biology and
1104   biomaterials for tissue engineering applications. *Journal of Industrial Microbiology and*
1105   *Biotechnology*, *45*(7), 599–614. https://doi.org/10.1007/s10295-018-2027-3
1106 Wolpert, L. (1969). Positional information and the spatial pattern of cellular differentiation.
1107   *Journal of Theoretical Biology*, *25*(1), 1–47. https://doi.org/10.1016/S0022-5193(69)80016-
1108   0
1109 Xia, P. F., Ling, H., Foo, J. L., & Chang, M. W. (2019). Synthetic genetic circuits for
1110   programmable biological functionalities. *Biotechnology Advances*, *37*(6), 107393.
1111   https://doi.org/10.1016/j.biotechadv.2019.04.015
1112 Xiong, L., Cao, Y., Cooper, R., Rappel, W. J., Hasty, J., & Tsimring, L. (2020). Flower-like
1113   patterns in multi-species bacterial colonies. *ELife*, *9*. https://doi.org/10.7554/eLife.48885
1114 Zong, D. M., Cinar, S., Shis, D. L., Josić, K., Ott, W., & Bennett, M. R. (2018). Predicting
1115   Transcriptional Output of Synthetic Multi-input Promoters. *ACS Synthetic Biology*, *7*(8),
1116   1834–1843. https://doi.org/10.1021/acssynbio.8b00165
1117